

Probing Hairy Kerr Black Holes through Quasi-Periodic Oscillations I: A study based on the kinematic models

Anirban Dasgupta^{a*}, Supragyan Priyadarshinee^{a,b†}, Indrani Banerjee^{a‡}, Subhash Mahapatra^{a§}

^a Department of Physics and Astronomy, National Institute of Technology Rourkela,
Rourkela - 769008, India

^b Department of Physics, IISER Mohali, Sector 81,
Knowledge City, Mohali, Punjab, 140306, India

Abstract

Black hole (BH) solutions endowed with nontrivial scalar or matter fields - commonly known as hairy black holes - have attracted significant interest in recent years. They admit extra parameters beyond mass, charge, and angular momentum, leading to a richer phenomenology. Characterizing their allowed parameter space is therefore crucial, especially in light of the available data from electromagnetic and gravitational-wave observations. The rotating hairy black hole solutions studied here are inspired by the gravitational decoupling method and satisfy the Einstein field equations with a conserved energy-momentum tensor that respects the strong energy conditions (SECs). We explore in detail the horizon structure of such black holes and report for the first time certain unique features, not observed in Kerr BHs. We investigate the sensitivity of the hairy parameters on the fundamental frequencies associated with the motion of matter in the hairy Kerr spacetime, and compare them with the Kerr scenario. The theoretical models aimed to explain the observed high-frequency observations (HFQPOs) in BHs are associated with the fundamental frequencies. Hence, such a study enables us to constrain the parameter space of the hairy Kerr spacetime by comparing the model-dependent HFQPO frequencies with the available observations. By comparing the kinematic models of HFQPOs with the observations of six BH sources, we report the most favored parameter space for each of these BHs. Our analysis also provides a framework to discern the most suitable model for each of these sources. Interestingly, even with the present precision of the data, the Relativistic Precession Model seems to be less suitable compared to the Tidal Disruption Model for the sources GRO J1655-40 and XTE J1859+226. The implications are discussed.

1 Introduction

Black holes, among the most mysterious objects in the Universe and remarkable predictions of general relativity, have attracted significant attention in recent decades. They naturally integrate key aspects of gravitational theory, thermodynamics, and quantum physics. Recent observational breakthroughs have further accelerated research in this area. Electromagnetic observations from satellites such as RXTE, Chandra, and NuSTAR, along with direct detections of gravitational waves by the LIGO–VIRGO collaboration [1–3], and the imaging of black hole shadows by the Event Horizon Telescope (EHT) [4,5], have enabled tests of gravity in the strong-field regime near the event horizon. These observations remain consistent with the predictions of general relativity.

Black hole solutions with nontrivial scalar or matter fields, commonly referred to as hairy black holes, have received considerable attention in recent years. Such solutions often arise in modified gravity theories, effective field models, or Einstein gravity coupled to additional fields with appropriate self-interactions. Unlike the no-hair results of classical general relativity [6–9], these configurations can possess additional parameters beyond mass, charge, and angular momentum, thereby enriching the phenomenology of compact objects. Understanding the allowed parameter space of hairy black holes is therefore essential, particularly in light of growing observational constraints from gravitational-wave detections and electromagnetic observations of

*522ph1007@nitrkl.ac.in

†supragyanpriyadarshinee52@gmail.com

‡banerjeein@nitrkl.ac.in

§mahapatrasub@nitrkl.ac.in

strong-gravity environments. For a recent discussion and comprehensive reviews on the existence of scalar hair in asymptotically flat spacetimes, see [10, 11]. Note that the no-hair conjecture lacks the rigor of a strict mathematical theorem, and a variety of counterexamples have been discovered over the years [12–28].

An interesting geometric framework for constructing hairy black hole solutions is gravitational decoupling, most notably implemented through the minimal geometric deformation (MGD) approach [29–33]. In this method, a known seed solution of Einstein’s equations is deformed by coupling it to an additional source sector via a controlled decoupling parameter. This technique has been successfully employed across a broad range of applications, including anisotropic stellar configurations [29, 34], wormholes [35], regular black holes [36–38], and a variety of hairy black hole geometries [31, 39]. A key strength of gravitational decoupling is that it enables the generation of new solutions without requiring an explicit matter Lagrangian for the additional sector.

Within the context of black holes, the decoupling parameter dictates the strength of the extra “hair” sector and thereby characterizes deviations from standard vacuum solutions such as Schwarzschild or Kerr. However, not all deformations yield physically viable spacetimes. Ensuring regularity outside the horizon, the existence of a well-defined event horizon, compliance with reasonable energy conditions, and thermodynamic consistency is essential. With increasingly precise observational probes, including gravitational-wave detections and black hole shadow measurements, it has become crucial to determine the regions of parameter space compatible with astrophysical constraints.

The extended gravitational decoupling framework [30, 31, 40–42] achieves a systematic modification of spherically symmetric backgrounds by adding new sources in such a way that Einstein’s equations decouple into separate sectors, allowing the deformed metric to be solved independently. Physical viability additionally requires the deformed geometry to satisfy the strong energy condition, remain free of extra singularities, and possess a well-defined horizon. Under these criteria, new static, spherically symmetric, asymptotically flat metrics were constructed in [31], and their rotating counterparts lead to hairy Kerr black holes characterized by deviation parameters α and l . The combination $l_0 = \alpha l$ plays a crucial role by modifying the thermodynamics and observational signatures of these objects [39]. These solutions have attracted significant theoretical and observational interest due to their improved dynamical stability and potential astrophysical relevance [31, 42, 43]. Observational constraints, particularly from the Event Horizon Telescope (EHT), have been used to set limits on the deformation parameter l and α [44]. These hairy Kerr solutions have therefore found successful applications in black hole thermodynamics [39, 45], gravitational lensing and shadow analysis [46], quasi-normal modes (QNMs) [47], gravitational-wave phenomenology, accretion disk physics [48–50], black hole spectroscopy [51], and parameter estimation using the EHT constraints [44, 52]. For other related works on hairy black holes, see [53–59]. The present work explores the horizon structure, the time-like geodesics and the fundamental frequencies associated with the hairy Kerr spacetime and reports some unique and interesting features which has not been previously reported to the best of our knowledge. Thereafter, we test the viability of the hairy Kerr spacetime in explaining the high-frequency quasi-periodic oscillations observed in certain black hole sources.

One of the most significant observational phenomena that characterizes strong gravitational interactions in the near-horizon region of black holes is the occurrence of Quasi-Periodic Oscillations (QPOs). These QPOs frequently appear as sharp peaks in the power-density spectra of certain black hole and neutron star sources and are commonly observed in their X-ray fluxes. Based on their observed frequencies, QPOs are conventionally classified into two categories: low-frequency QPOs (LFQPOs), with frequencies in the mHz range, and high-frequency QPOs (HFQPOs), which typically occur at a few hundred hertz in stellar-mass black hole (BH) systems [60, 61]. Observational confirmation of HFQPOs was first achieved with NASA’s Rossi X-Ray Timing Explorer satellite [62]. The present work is concerned with HFQPOs in BH sources [63–66]. In low-mass X-ray binaries (LMXRBs), HFQPOs correspond to characteristic timescales of 0.1–1 ms, which are commensurate with the dynamical timescales of accreting matter in the innermost regions ($r < 10R_g$) of compact objects [67–69]. Such millisecond dynamical timescales for stellar-mass BHs [67, 68] correspond to Fourier-domain frequencies of a few hundred hertz, consistent with observed HFQPOs [60, 70]. This agreement underscores the physical relevance of HFQPOs as diagnostics of accretion dynamics and strong-field gravity in the vicinity of BHs [60].

Because HFQPO frequencies are closely associated with the orbital and epicyclic frequencies of matter near the compact object, they exhibit an inverse scaling with the mass of the central object. Consequently, HFQPOs occur at kHz frequencies in neutron-star systems, whereas in supermassive BHs—for example, Sgr A*, they are shifted to the mHz range. Owing to their intrinsic connection to the motion of accreting matter in the immediate vicinity of compact objects, HFQPOs are believed to encode crucial information about gravity

in the strong-field, high-curvature regime [69]. Their investigation therefore offers a distinctive observational probe of near-horizon physics and the fundamental properties of BH spacetimes and several theoretical studies have delved into this field [71–75]. In the present work we test the hairy Kerr spacetime with the available HFQPO data of the six BH sources assuming the kinematic models for the HFQPOs. A similar study has been done previously [76] where only one of the available kinematic models was considered and the parameter space seemingly has not been exhaustively explored. The present work analyses the parameter space more comprehensively and therefore offers to bridge this gap in the literature.

The paper is organized as follows: In Sec. 2 we provide an overview of the rotating hairy Kerr BH spacetime and discuss its horizon structure. We investigate the nature of time-like geodesics and the fundamental frequencies associated with the hairy Kerr spacetime in Sec. 3. Sec. 4 is dedicated to test the viability of the hairy Kerr spacetime in explaining the observed HFQPOs of BHs in the context of the available kinematic models. A comparison between the different HFQPO models is performed to test the suitability of each of these models source-wise. We summarize the constraints obtained on the deformation parameter and the length parameter, discuss their implications, and conclude with some scope for future work in Sec. 5. We work with mostly positive metric convention and consider geometrized units, i.e., $G = c = 1$.

2 A brief review of the rotating hairy solutions

In this section, we briefly review the rotating hairy black hole (BH) solution which is a solution of Einstein field equations with a conserved energy-momentum (EM) tensor that satisfies the strong energy conditions (SECs). This conserved energy-momentum tensor takes into account one or more fundamental fields (which may be of scalar, vector, or tensor origin) arising due to the presence of dark-matter and/or dark-energy, whose nature is unknown. This EM tensor needs to fulfill only certain minimal conditions, namely, (i) should be well-behaved everywhere outside the event horizon, (ii) should fulfill the strong-energy conditions outside the event horizon, and (iii) the resultant hairy metric should possess a well-defined event horizon. The rotating hairy black hole solution can be obtained by first applying the extended gravitational decoupling method [31, 42] to generate the static hairy black hole background [29, 30], and subsequently employing the Newman–Janis algorithm [39]. The static seed metric for this construction is given by

$$ds^2 = -\left(1 - \frac{2\mathcal{M}}{r} + \alpha e^{\frac{-r}{\mathcal{M}-\alpha l/2}}\right)dt^2 + \left(1 - \frac{2\mathcal{M}}{r} + \alpha e^{\frac{-r}{\mathcal{M}-\alpha l/2}}\right)^{-1}dr^2 + r^2d\Omega^2, \quad (2.1)$$

where α is the deviation parameter measuring deviation from the Schwarzschild metric, $l_0 = \alpha l$ corresponds to the primary hair, and \mathcal{M} is associated with the ADM mass of the black hole. This is the mass that will be observed by an asymptotic observer at infinity and is related to the usual Schwarzschild mass M by the relation $\mathcal{M} = M + \alpha l/2$.

To constrain the parameters of the hairy black hole and test their physical validity, it is crucial to obtain their rotating counterparts. Since the black hole spin is crucial in astrophysical processes, it makes rotating black holes important as they provide prototypes of black holes that are usually observed in nature. The axisymmetric and stationary counterpart of the above spherically symmetric static solution in Boyer-Lindquist coordinates reads [39, 42],

$$ds^2 = g_{tt}(r, \theta)dt^2 + 2g_{t\varphi}(r, \theta)dtd\varphi + g_{\varphi\varphi}(r, \theta)d\varphi^2 + g_{rr}(r, \theta)dr^2 + g_{\theta\theta}(r, \theta)d\theta^2, \quad (2.2)$$

where

$$\begin{aligned} g_{tt}(r, \theta) &= -\frac{r^2(1 - 2\mathcal{M}/r + \alpha e^{-r/(\mathcal{M}-\alpha l/2)}) + a^2 \cos^2 \theta}{\Sigma}, \\ g_{t\varphi}(r, \theta) &= -\frac{ar^2 \sin^2 \theta \left(\frac{2\mathcal{M}}{r} - \alpha e^{-r/(\mathcal{M}-\alpha l/2)}\right)}{\Sigma}, \\ g_{\varphi\varphi}(r, \theta) &= \Sigma \sin^2 \theta \left[1 + a^2 \sin^2 \theta \frac{r^2(1 + 2\mathcal{M}/r - \alpha e^{-r/(\mathcal{M}-\alpha l/2)}) + a^2 \cos^2 \theta}{\Sigma^2}\right], \\ g_{rr}(r, \theta) &= \frac{\Sigma}{a^2 + r^2(1 - 2\mathcal{M}/r + \alpha e^{-r/(\mathcal{M}-\alpha l/2)})}, \\ g_{\theta\theta}(r, \theta) &= \Sigma, \end{aligned} \quad (2.3)$$

with $\Sigma = r^2 + a^2 \cos^2 \theta$. Notice that all metric coefficients, except the $g_{\theta\theta}$ term, receive corrections due to the deviation and the hair parameter. As expected, in the limit $\alpha \rightarrow 0$ (vanishing deviation), this new axisymmetric hairy black hole solution reduces to the Kerr geometry and approaches the Schwarzschild geometry with mass \mathcal{M} when the spin a also vanishes. Note that in order to ensure asymptotic flatness of Eq. 2.3, $\alpha l \leq 2$ is necessary, and one can show that the Kerr solution is again recovered when $\alpha l = 2$. This hairy black hole solution (Eq. 2.2) results from the matter energy-momentum tensor that satisfies the strong energy condition and is the prototype of non-Kerr black holes with additional hairy parameters $\{\alpha, l\}$. Note that when α is non-zero but l vanishes, the resultant static or stationary BH solution has no GR counterpart. We will show below that such a geometry originates from an effective EM tensor that violates the strong energy condition. Consequently, the $l = 0$ branch will not be considered when discussing observational constraints.

The EM tensor associated with the above-mentioned rotating hairy BH solution is given by

$$T^{\mu\nu} = \tilde{\rho} e_t^\mu e_t^\nu + \tilde{p}_r e_r^\mu e_r^\nu + \tilde{p}_\theta e_\theta^\mu e_\theta^\nu + \tilde{p}_\phi e_\phi^\mu e_\phi^\nu, \quad (2.4)$$

where

$$\begin{aligned} e_t^\mu &= \frac{(r^2 + a^2, 0, 0, a)}{\sqrt{\Sigma\Delta}}, & e_r^\mu &= \frac{\sqrt{\Delta}(0, 1, 0, 0)}{\sqrt{\Sigma}}, \\ e_\theta^\mu &= \frac{(0, 0, 1, 0)}{\sqrt{\Sigma}}, & e_\phi^\mu &= \frac{(a \sin^2 \theta, 0, 0, 1)}{\sqrt{\Sigma} \sin \theta}, \end{aligned} \quad (2.5)$$

are the tetrads with $\Delta = a^2 + r^2(1 - 2\mathcal{M}/r + \alpha e^{-r/(\mathcal{M}-\alpha l/2)})$ and $\tilde{\rho}$ is the energy density while $\tilde{p}_r, \tilde{p}_\theta, \tilde{p}_\phi$ are the pressures. The energy density and pressures giving rise to the hairy BH solution are given by [39],

$$\begin{aligned} \tilde{\rho} &= \frac{\alpha r^2 e^{-\frac{r}{\mathcal{M}-\frac{\alpha l}{2}}}}{\kappa^2 \Sigma^2 (\mathcal{M} - \frac{\alpha l}{2})} \{r - (\mathcal{M} - \frac{\alpha l}{2})\}, \\ \tilde{p}_r &= -\tilde{\rho}, \\ \tilde{p}_\theta &= \frac{\alpha r^2 e^{-\frac{r}{\mathcal{M}-\frac{\alpha l}{2}}}}{\kappa^2 \Sigma^2 (\mathcal{M} - \frac{\alpha l}{2})} \{r - (\mathcal{M} - \frac{\alpha l}{2})\} + \frac{\alpha e^{-\frac{r}{\mathcal{M}-\frac{\alpha l}{2}}}}{2\kappa^2 (\mathcal{M} - \frac{\alpha l}{2})^2 \Sigma} \{2(\mathcal{M} - \frac{\alpha l}{2})^2 - 4(\mathcal{M} - \frac{\alpha l}{2})r + r^2\}, \\ \tilde{p}_\phi &= \tilde{p}_\theta. \end{aligned} \quad (2.6)$$

In order to fulfill the strong energy conditions, one needs to ensure that the energy density and pressures discussed above satisfy,

$$\tilde{\rho} + \tilde{p}_r + 2\tilde{p}_\theta \geq 0, \quad \tilde{\rho} + \tilde{p}_r \geq 0, \quad \tilde{\rho} + \tilde{p}_\theta \geq 0. \quad (2.7)$$

In order for the energy density and pressures in Eq. 2.6 to satisfy the strong energy conditions we need to ensure that: (a) $\tilde{\rho} \geq 0$ and $\tilde{p}_\theta \geq 0$. Throughout this paper we will consider motion in the equatorial plane, such that positivity of $\tilde{\rho}$ and \tilde{p}_θ respectively requires,

$$r > \mathcal{M} - \frac{\alpha l}{2}, \quad (2.8)$$

$$r > 2(\mathcal{M} - \frac{\alpha l}{2}). \quad (2.9)$$

In what follows we will scale the length parameter l , the angular momentum of the black hole a and the distance r with the ADM mass \mathcal{M} , such that $l \equiv \frac{l}{\mathcal{M}}$, $a \equiv \frac{a}{\mathcal{M}}$ and $r \equiv \frac{r}{\mathcal{M}}$. We need to ensure that the strong energy conditions are satisfied everywhere outside the event horizon which requires $r \geq r_{SEC}$ where $r_{SEC} = 2(1 - \frac{\alpha l}{2})$. Note that r_{SEC} does not depend on the rotation of the black hole.

The event horizon is obtained by solving for the roots of $g^{rr} = \Delta = 0$, which mostly yield two solutions, but sometimes up to four solutions, depending on the choice of l , α , and a . The horizon structure of the rotating hairy BH has been discussed earlier [39, 44, 46], here we highlight some of the additional features of the horizon that have not been mentioned before, to the best of our knowledge. Analysis of the horizon structure requires one to plot Δ with the radial distance r . Further, one needs to ensure that the outer horizon $r_{EH} > r_{SEC}$, based on which three scenarios emerge, which we discuss below:

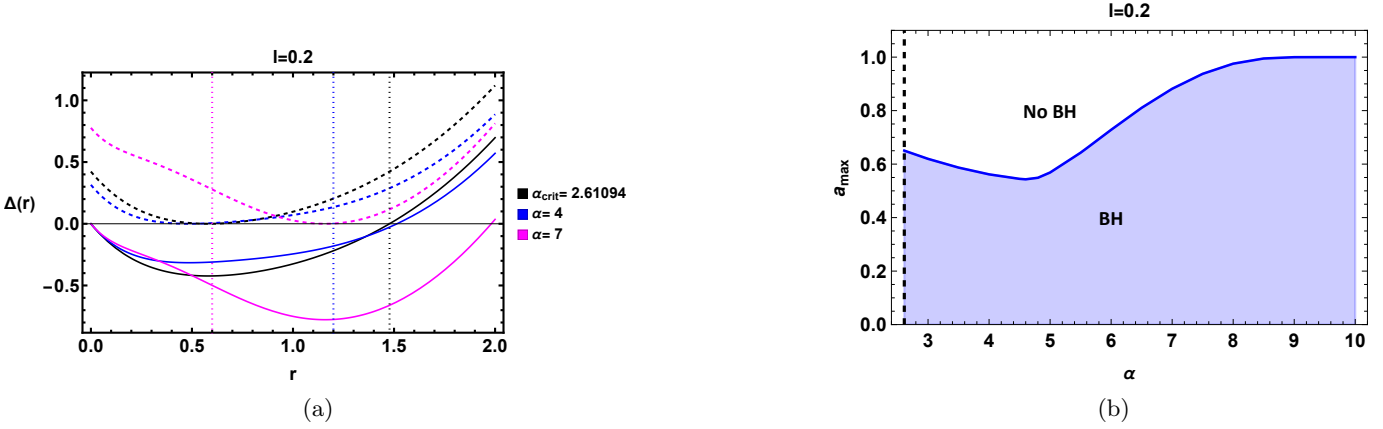


Figure 1: In the figure above, we consider the case $l = 0.2$. Figure (a) shows the variation of $\Delta(r)$ for different values of α : $\alpha = \alpha_{crit}$, $\alpha = 4$ (which lies between α_{crit} and α_{coin}), and $\alpha = 7$ (which is greater than α_{coin}). The solid curves correspond to the non-rotating case $a = 0$, while the dashed curves represent the extremal cases $a = a_{max}$, for which $\Delta(r)$ develops a coincident root. For each value of α , the vertical dotted line marks the position $r = r_{SEC}$, indicating the radius at which the strong energy condition begins to fail. Figure (b) shows, for the same choice $l = 0.2$, the maximum spin parameter a_{SEC} allowed by the SEC as a function of α , for the interval $\alpha_{crit} \leq \alpha \leq \alpha_{max}$.

2.1 Case $l > e^{-2}$:

Just like the Kerr BH, a hairy black hole with a given (l, α) has the largest horizon when its spin is zero. As spin increases the outer horizon decreases while the inner horizon increases until they coincide at a_{max} , which is the extremal BH scenario. Thus, for a given (l, α) if $r_{SEC} > r_{EH}$ for the non-rotating case then the SEC is violated for all higher spin BHs.

- For a given l (with $l > e^{-2}$) as we increase α , r_{SEC} decreases and the critical α (denoted by α_{crit}) is obtained when r_{SEC} coincides with the horizon radius of the static BH. Thus,

$$\alpha_{crit} = \frac{2}{l} - e^2 \quad (2.10)$$

which is obtained by solving $\Delta(r_{SEC}) = 0$ for α and l assuming $a = 0$. For a given $l > e^{-2}$, α_{crit} vanishes when $l \simeq 2/e^2$. Thus when $l > 2/e^2$, SEC is satisfied for all allowed α , i.e., between $0 \lesssim \alpha \lesssim \alpha_{max} = \frac{2}{l}$.

- For a given l , if $\alpha < \alpha_{crit}$ then the SEC is not satisfied. Hence, we will confine ourselves only to the cases where $\alpha \geq \alpha_{crit}$. At $\alpha = \alpha_{crit}$ only the static BH satisfies the SEC. Thus, BHs with $|a| > 0$ will not be considered in this case. Note that for a given (l, α) , $0 \leq |a| \leq a_{max}$, where a_{max} corresponds to the extremal BH which is obtained by solving $\Delta(l, \alpha, a, r) = \Delta'(l, \alpha, a, r) = 0$.
- When $\alpha_{crit} \leq \alpha \leq \alpha_{coin}$, where $\alpha_{coin} = \frac{1}{l}$, BHs with any allowed spin between $0 \leq a \leq a_{max}$ do not satisfy the SEC. The spin up to which SEC holds good is given by a_{SEC} ,

$$a_{SEC} = \sqrt{2r_{SEC} - r_{SEC}^2(1 + \alpha e^{-2})} \quad (2.11)$$

which is obtained by solving $\Delta(r_{SEC}) = 0$ for a , for fixed (l, α) .

- When $\alpha = \alpha_{coin}$, r_{SEC} corresponds to the horizon radius of the extremal BH, i.e., when one solves $\Delta(l, \alpha, a, r_{SEC}) = \Delta'(l, \alpha, a, r_{SEC}) = 0$, one arrives at $\alpha_{coin} = \frac{1}{l}$ and $a_{SEC} = a_{max}$. Thereafter, as we consider $\alpha > \alpha_{coin}$, BHs with all allowed values of spin satisfy the SEC. Note that we cannot have $\alpha > \alpha_{max} = \frac{2}{l}$, otherwise asymptotic flatness would not be ensured.
- Thus, to summarize, for values of $l > e^{-2}$, when $\alpha_{crit} \leq \alpha \leq \alpha_{coin}$ the spin range is $0 \leq |a| \leq a_{SEC}$, while when $\alpha_{coin} < \alpha \leq \alpha_{max}$ the spin range is $0 \leq |a| \leq a_{max}$ and Δ always has two real roots.

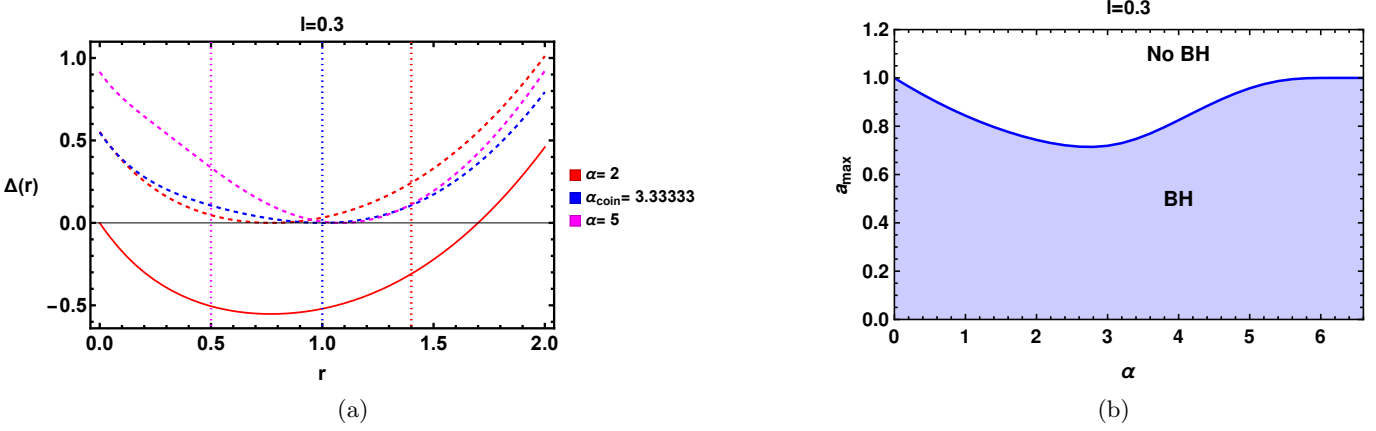


Figure 2: In the figure above, we consider the case $l = 0.3$. Figure (a) illustrates the behavior of $\Delta(r)$ for several representative values of α , ranging from $\alpha < \alpha_{\text{coin}}$ ($\alpha = 2$), $\alpha = \alpha_{\text{coin}}$, and $\alpha > \alpha_{\text{coin}}$ ($\alpha = 5$). Solid curves denote the non-rotating configurations $a = 0$, while the dotted curves correspond to the extremal cases $a = a_{\text{max}}$, where $\Delta(r)$ develops a coincident root. For each α , the vertical dotted line marks the radius $r = r_{\text{SEC}}$ at which the strong energy condition ceases to hold. Figure (b) shows, for the same choice $l = 0.3$, the maximum spin parameter allowed by the strong energy condition as a function of α , for the range $0 \leq \alpha \leq \alpha_{\text{max}}$.

[Fig. 1](#) and [Fig. 2](#) show the variation of Δ with r for various choices of α and a for $l = 0.2$ and $l = 0.3$, respectively. In these figures, corresponding to each choice of α , the solid lines are used to represent the $a = 0$ cases while the dotted lines are used to denote the $a = a_{\text{max}}$ (corresponding to a given α, l) cases. The Δ corresponding to α_{crit} is plotted with black color. For $l = 0.3$, $\alpha_{\text{crit}} < 0$ hence it is not shown in [Fig. 2a](#) and in these kind of cases all values of α between 0 to α_{max} are allowed. The vertical dotted lines in these figures denote r_{SEC} corresponding to a given choice of α and l .

For $l = 0.2$, the critical value of the deformation parameter is $\alpha_{\text{crit}} \simeq 2.6109$, at which the outer horizon of the non-rotating black hole coincides with r_{SEC} . Equivalently, at this critical point the zero of $\Delta(r)$ aligns exactly with r_{SEC} , as indicated by the black vertical dotted line. Clearly for $\alpha = \alpha_{\text{crit}}$, the SEC is immediately violated once rotation is introduced ($|a| > 0$), which is evident in [Fig. 1a](#), where the black dashed curve (corresponding to $a = a_{\text{max}}$) has coincident roots at radii smaller than r_{SEC} . The blue curves in [Fig. 1a](#) correspond to $\alpha = 4$, a value between α_{crit} and α_{coin} . Here the SEC holds for the static case ($a = 0$) but fails for the extremal rotating case, as indicated by the blue vertical dotted line lying between the zero crossings of the blue solid and blue dashed curves. In contrast, for $\alpha = 7 > \alpha_{\text{coin}}$ (shown by the magenta curves in [Fig. 1a](#)), the SEC is satisfied for all allowed spins $0 \leq a \leq a_{\text{max}}$, since the magenta vertical dotted line marking r_{SEC} lies to the left of the zero crossings of both corresponding $\Delta(r)$ curves.

In [Fig. 2](#) (for $l = 0.3$), the SEC is satisfied for $0 \leq a \leq a_{\text{SEC}}$ when $\alpha = 2$, but it fails at $a = a_{\text{max}}$. At $\alpha_{\text{coin}} \simeq 3.33$, the SEC becomes satisfied across the entire spin range $0 \leq a \leq a_{\text{max}}$; the blue dotted vertical line marks the radius where the corresponding $\Delta(r)$ curve develops a coincident root. Since $r_{\text{SEC}} \leq r_{\text{EH}}$ at $a = a_{\text{max}}$ implies the same for all lower spins, the $a = 0$ cases are omitted for $\alpha \geq \alpha_{\text{coin}}$. For $\alpha > \alpha_{\text{coin}}$ (e.g., $\alpha = 5$ in [Fig. 2a](#)), the SEC is satisfied for all allowed spins, as illustrated in [Fig. 2a](#).

In [Fig. 1b](#) and [Fig. 2b](#), we show the maximum allowed spin as a function of α within the admissible range $\alpha_{\text{crit}} \leq \alpha \leq \alpha_{\text{max}}$ for $l = 0.2$ and $l = 0.3$, respectively. In [Fig. 1b](#), α_{crit} is indicated by the black dashed vertical line, whereas it does not appear in [Fig. 2b](#) because it lies at a negative value of α , and $\alpha < 0$ is not allowed [31]. For any fixed l and α , increasing the spin beyond a_{max} makes the horizon imaginary, resulting in a naked singularity. Since we are interested only in black hole solutions (the blue shaded regions in [Fig. 1b](#) and [Fig. 2b](#)), we will only focus in the regime $0 \leq |a| \leq a_{\text{max}}$ for a given l, α in subsequent analysis.

2.2 Case $l = e^{-2}$:

In the case $l > e^{-2}$, we observed that for $\alpha_{\text{crit}} \leq \alpha \leq \alpha_{\text{coin}}$, the extremal black holes do not satisfy the SEC. However, as l is decreased to the limiting value $l = e^{-2}$, the parameter α_{coin} coincides with α_{crit} . The implications of this coincidence, and its impact on the SEC behavior and the structure of extremal solutions, are discussed below.

- In this case, $\alpha_{crit} = \alpha_{coin} = e^2$, which implies that only the region $\alpha > e^2$ should be considered for the SEC to be satisfied.
- For completeness, we note that when $\alpha < e^2$ and $0 < a < a_{max}$, the function $\Delta(r)$ has two real roots, which coincide when $a = a_{max}$.
- When $\alpha = e^2$, the non-rotating BH also happens to be the extremal BH, hence $|a| > 0$ should not be considered.
- For this value of l , when $\alpha = e^2$ and $a = 0$, the event horizon corresponds to the inflection point of Δ and coincides with r_{SEC} , i.e., $\Delta(r_{EH}) = \Delta'(r_{EH}) = \Delta''(r_{EH}) = 0$ with $r_{EH} = r_{SEC} = 2(1 - \frac{\alpha l}{2})$.
- When $\alpha \geq e^2$, the extremal BH condition is achieved at a higher value of spin, and for all spins between $0 \leq a \leq a_{max}$, the strong energy condition holds, meaning that $r_{SEC} < r_{EH}$. Therefore, the SEC is satisfied throughout the entire allowed spin range, unlike in the previous case.
- For $e^2 < \alpha < 8.15$ and $a = a_{max}$, Δ admits three real roots, with the two inner roots becoming coincident when $\alpha \simeq 8.15$. For α above this value, $\Delta(a_{max})$ possesses only one real root. In this range of α , and for certain choices of the spin parameter, Δ can have four real roots. However, we do not discuss these additional roots in detail, as our main interest lies in the outer root, which always remains greater than r_{SEC} .
- When $\alpha \gtrsim 9.5$ and $0 \leq a \leq a_{max}$, Δ again exhibits two real roots. As α increases further, the hairy black hole begins to resemble the horizon structure of the Kerr black hole.
- Once again, we cannot increase α beyond $\alpha_{max} = 2e^2$. Therefore, in this case the allowed range of the deviation parameter is $e^2 \leq \alpha \leq 2e^2$, and for every value of α within this interval, the entire range of spin is permitted.

The above features are most clearly demonstrated in [Fig. 3a](#), which shows the behavior of $\Delta(r)$ for $l = e^{-2}$ and different values of α . As before, the solid and dotted curves correspond to $a = 0$ and $a = a_{max}$ respectively, and the vertical dotted lines mark the associated r_{SEC} . For this choice of l , the critical value is $\alpha_{crit} = e^2$, for which $r_{EH} = r_{SEC}$ and $a_{max} = 0$. At this point, $\Delta(r)$ develops an inflection at the horizon, as shown by the black solid curve. When $\alpha < \alpha_{crit}$ (e.g., $\alpha = 5$), the SEC fails for all spins, since the corresponding r_{SEC} lies outside the outer horizon already at $a = 0$, and the horizon radius decreases with spin. For $\alpha > \alpha_{crit}$, the allowed spin increases from zero, and the SEC is satisfied for every $0 \leq a \leq a_{max}$. In the interval $e^2 < \alpha \lesssim 8.15$, $\Delta(r) = 0$ admits four real roots for $a < a_{max}$, while the extremal geometry ($a = a_{max}$) exhibits three roots with a double outer root. Near $\alpha \simeq 8.15$, the two inner roots merge for $a < a_{max}$, and for $a = a_{max}$ the outer roots also become coincident, as seen from the magenta dashed curve. For $\alpha > 8.15$, the structure simplifies: $\Delta(r) = 0$ yields two real roots for $a < a_{max}$ and a single degenerate root at extremality, resembling the Kerr limit. This trend is expected, since increasing α toward $\alpha_{max} = 2/l$ restores asymptotic flatness.

[Fig. 3b](#) shows how a_{max} varies with α in the range $\alpha_{crit} \leq \alpha \leq \alpha_{max}$ for $l = e^{-2}$, where α_{crit} is indicated by the black dashed line. Consistent with the previous analysis, $a_{max} = 0$ at the critical value $\alpha = \alpha_{crit} = e^2$, meaning that the non-rotating black hole is already extremal at this point.

2.3 Case $l < e^{-2}$:

When $l < e^{-2}$ and α lies below a critical threshold α_{crit} , the SEC is violated since $r_{EH} < r_{SEC}$. This behavior is illustrated for $l = 0.1$ in [Fig. 4a](#). For $\alpha < \alpha_{crit}$ (with $\alpha_{crit} \simeq 11.484$ for this choice of l), the function $\Delta(r)$ admits two real roots, but both lie inside r_{SEC} . This is seen for $\alpha = 10$ and $a = 0$ (purple solid curve), where the outer horizon remains smaller than the SEC threshold (purple vertical line). Since a violation of the SEC already occurs for $a = 0$, increasing the spin cannot restore it, and therefore other spin values are not shown for $\alpha = 10$. At the critical value $\alpha = \alpha_{crit} \simeq 11.484$, $\Delta(r)$ at $a = 0$ develops three real roots (black solid curve), with the outermost horizon becoming a coincident root and shifting beyond r_{SEC} (black dotted vertical line). This implies that:

- Once again, the critical α corresponds to the case when the non-rotating BH is also the extremal BH, but unlike the previous case, now $r_{EH} > r_{SEC}$. Note that, this BH has two inner horizons with radii less than r_{SEC} , which are not important from an observational point of view.

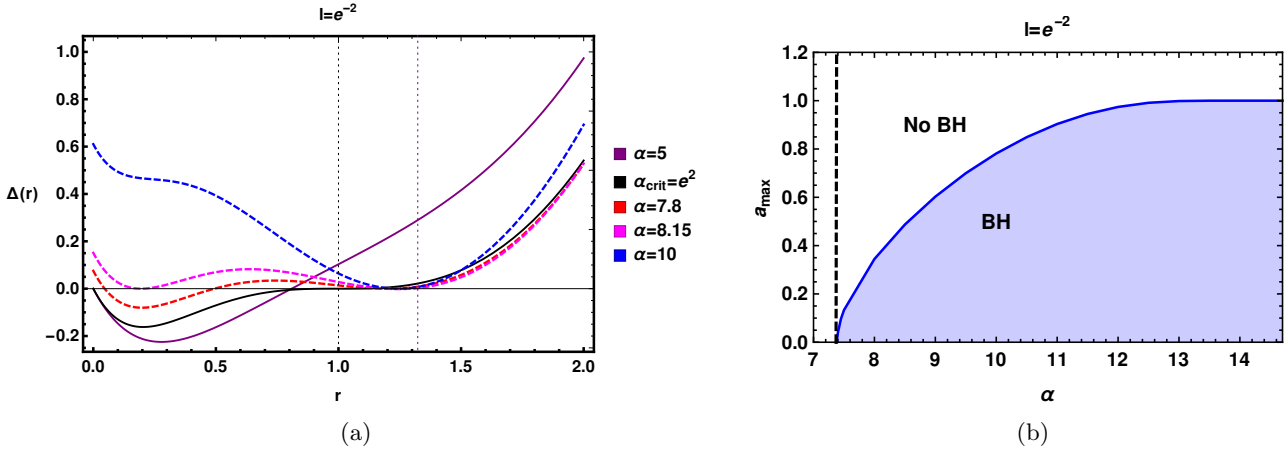


Figure 3: In the figure above, we consider the case $l = e^{-2}$. Figure (a) shows the behavior of $\Delta(r)$ for several values of α , including $\alpha < \alpha_{crit}$ ($\alpha = 5$), the critical case $\alpha = \alpha_{crit} = e^2$, and values $\alpha > \alpha_{crit}$ ($\alpha = 7.8, 8.15, 10$). Solid curves represent the non-rotating case $a = 0$, while dashed curves correspond to the extremal configurations $a = a_{max}$. The vertical dotted lines indicate $r = r_{SEC}$ for each choice of α . Figure (b) displays the corresponding dependence of the maximum allowed spin a_{max} on α within the interval $\alpha_{crit} \leq \alpha \leq a_{max}$.

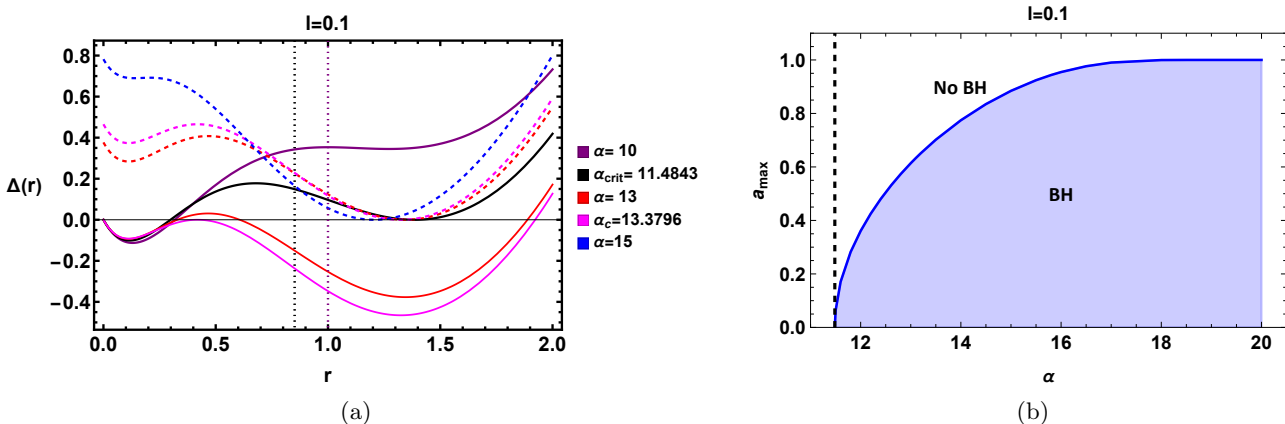


Figure 4: In the figure above, we consider the case $l = 0.1 < e^{-2}$. Figure (a) shows the behavior of $\Delta(r)$ for several values of α , including $\alpha < \alpha_{crit}$ ($\alpha = 10$), the critical case $\alpha = \alpha_{crit}$, and values $\alpha > \alpha_{crit}$ ($\alpha = 13, \alpha_c, 15$). Solid curves represent the non-rotating case $a = 0$, while dashed curves correspond to the extremal configurations $a = a_{max}$. The vertical dotted lines indicate $r = r_{SEC}$ for each choice of α . Figure (b) displays the corresponding dependence of the maximum allowed spin a_{max} on α within the interval $\alpha_{crit} \leq \alpha \leq a_{max}$.

- The critical α_{crit} is obtained by solving $\Delta(r_{EH}) = \Delta'(r_{EH}) = 0$ with $a = 0$ which gives us the radii of the coincident roots of Δ ,

$$r_{h\pm} = 1 \pm \sqrt{\alpha l - 1}. \quad (2.12)$$

The critical α for a given $l < e^{-2}$ is obtained by substituting r_{h+} in $\Delta = 0$ with $a = 0$ and solving for α . This requires solving the following equation:

$$\alpha e^{-\frac{r_{h+}}{1-\frac{\alpha l}{2}}} = \frac{2}{r_{h+}} - 1, \quad (2.13)$$

for a given l .

- For $\alpha_{crit} < \alpha < \alpha_c$ and for certain spins between $0 \leq a < a_{max}$, Δ has four real roots with the largest root $r_{EH} > r_{SEC}$. Such a situation corresponds to $\alpha = 13$ and $a = 0$ (the red solid curve in Fig. 4a).

The red dashed curve in [Fig. 4a](#) is associated with $a = a_{max}$ (extremal BH case) for $\alpha = 13$, which does not have 4 real roots of $\Delta(r)$. The inner roots are however not relevant astrophysically. The important thing to note is that, BHs with any allowed spin with $\alpha > \alpha_{crit}$ satisfies the SEC anywhere outside the outer horizon, i.e., $r_{EH} > r_{SEC}$. Here α_c is obtained when r_{h_-} in [Eq. 2.12](#) is substituted in $\Delta = 0$ with $a = 0$, i.e., using r_{h_-} in [Eq. 2.13](#) instead of r_{h_+} and solving for α for a given $l < e^{-2}$.

- When $\alpha = \alpha_c \simeq 13.3796$ (for $l = 0.1$) the inner roots of $\Delta(r)$ coincide for $a = 0$, which is evident from the solid magenta curve in [Fig. 4a](#). For higher spin values, but $a < a_{max}$, there are two real roots for Δ , while a single coincident root arises for $a = a_{max}$ as illustrated by the magenta dashed curve in [Fig. 4a](#).
- As α is gradually increased beyond α_c (e.g. $\alpha = 15$ and $a = a_{max}$, denoted by the blue dashed curve in [Fig. 4a](#)), the larger spins first begin to mimic the Kerr-like behavior of Δ (two real roots) followed by smaller spins.
- Overall, for $l < e^{-2}$, when the deviation parameter is between $\alpha_{crit} \leq \alpha \leq \alpha_{max}$, the SEC is satisfied for any r outside the event horizon for any allowed range of spin. Finally as $\alpha \rightarrow \alpha_{max} = \frac{2}{l}$ we recover the Kerr scenario.

In [Fig. 4b](#), we plot the variation of a_{max} with α for $l = 0.1$. Here, α_{crit} is shown with the black dashed vertical line. It shows that at α_{crit} , the non-rotating BH is also the extremal BH. The above discussion elucidates that the non-trivial features of hairy Kerr BH become apparent for smaller values of $0 < l \leq e^{-2}$ with $\alpha \gtrsim \alpha_{crit}$ but much less than α_{max} . We also note that for a fixed l , one may in principle consider $\alpha < \alpha_{crit}$, provided the region of interest remains outside the radius r_{SEC} associated with that parameter set (see [Eq. 2.9](#)).

We end this section by pointing out that the case $l = 0$ is ruled out, since the resulting geometry admits only two horizons, both lying well inside $r_{SEC} = 2$, and therefore fails to satisfy the SEC at all points outside the outer horizon. Thus, to bring out the non-trivial horizon structures of the hairy Kerr BH we need both non-vanishing l and α .

3 Epicyclic frequencies for hairy black holes

The stationary, axisymmetric spacetime described by the hairy Kerr metric has the general form:

$$ds^2 = g_{tt}dt^2 + 2g_{t\phi}dtd\phi + g_{\phi\phi}d\phi^2 + g_{rr}dr^2 + g_{\theta\theta}d\theta^2, \quad (3.1)$$

where $g_{\nu\mu} = g_{\mu\nu}(r, \theta)$ and $g_{\nu\mu}(r, \theta) = g_{\nu\mu}(r, -\theta)$. Here, we consider the motion of massive test particles around such a spacetime. When we study the Lagrangian we get two conserved quantities here. The first one is the energy E per unit mass, and the second one is the angular momentum L per unit mass. Now, the Lagrangian is

$$\mathcal{L} = g_{tt}\dot{t}^2 + 2g_{t\phi}\dot{t}\dot{\phi} + g_{\phi\phi}\dot{\phi}^2 + g_{rr}\dot{r}^2 + g_{\theta\theta}\dot{\theta}^2. \quad (3.2)$$

From the Euler-Lagrangian equation, we get

$$\frac{d}{d\lambda}\left(\frac{\partial\mathcal{L}}{\partial\dot{t}}\right) - \frac{\partial\mathcal{L}}{\partial t} = 0. \quad (3.3)$$

Since $\frac{\partial\mathcal{L}}{\partial t} = 0$, as \mathcal{L} is independent of t , we have $\frac{\partial\mathcal{L}}{\partial\dot{t}} = -2E = \text{constant}$. This leads to

$$g_{tt}\dot{t} + g_{t\phi}\dot{\phi} = -E = p_t. \quad (3.4)$$

Now, \mathcal{L} is also independent of ϕ , which implies $\frac{\partial\mathcal{L}}{\partial\dot{\phi}} = -2L = \text{constant}$. From this, we get

$$g_{\phi\phi}\dot{\phi} + g_{t\phi}\dot{t} = L = p_\phi. \quad (3.5)$$

From the above two conserved quantities, we can determine the potential under whose influence the test particle is rotating,

$$U(r, \theta) = g^{tt} - 2\left(\frac{L}{E}\right)g^{t\phi} + \left(\frac{L}{E}\right)^2g^{\phi\phi}. \quad (3.6)$$

From $g_{\mu\nu}u^\mu u^\nu = -1$, we also have

$$g_{rr}\dot{r}^2 + g_{\theta\theta}\dot{\theta}^2 + E^2U(r, \theta) = -1. \quad (3.7)$$

Since we restrict the test particle motion to the equatorial plane, the above equation reduces to $\dot{r}^2 = V(r)$, where the effective potential is given by $V(r) = -\frac{1+E^2U(r_c, \frac{\pi}{2})}{g_{rr}}$.

The marginally stable circular orbit can be obtained from $V(r) = 0$, $V'(r) = 0$, and $V''(r) = 0$. This is the last stable orbit where the particle can move in a circular path. After that, it will fall radially towards the black hole. As the particle moves along a circular orbit around the black hole, it acquires a corresponding angular velocity $\Omega = \frac{u^\phi}{u^t}$, where $u^\mu = \dot{x}^\mu = \frac{dx^\mu}{d\tau}$. From the radial Euler-Lagrangian equation and by considering circular, equatorial geodesics, we obtain

$$\frac{\partial g_{tt}}{\partial r} + 2\Omega\frac{\partial g_{t\phi}}{\partial r} + \Omega^2\frac{\partial g_{\phi\phi}}{\partial r} = 0. \quad (3.8)$$

We get Ω by solving the above quadratic equation,

$$\Omega = \frac{-\partial_r g_{t\phi} \pm \sqrt{(\partial_r g_{t\phi})^2 - (\partial_r g_{\phi\phi})(\partial_r g_{tt})}}{\partial_r g_{\phi\phi}}, \quad (3.9)$$

where $\Omega = 2\pi f_\phi$, with f_ϕ being the frequency with which the test particle is rotating around the black hole.

In Fig. 5, we plot the variation of f_ϕ with r for different choices of l , α and a . Here we mainly show variation with respect to α and a for a fixed l . In each row, we consider a fixed l but allow variation with respect to α . Panel (a) shows the Kerr case with $\alpha = 0$, where f_ϕ is plotted from $a = -a_{max}$ to $a = a_{max}$. In panels (b)-(c), we fix $l = 0.1$ ($l < e^{-2}$) and vary α as 12 and 14, respectively. Next, we fix $l = e^{-2}$ and vary α in panels (e)-(f). Finally, we consider $l = 0.3$ ($l > e^{-2}$) and vary α in panels (h)-(i) of Fig. 5.

From Fig. 5 we note that for a fixed l and α , f_ϕ increases upto the r_{ms} as one moves closer to the black hole and also upon decreasing the black hole spin. Such a trend is also observed in the Kerr case. The vertical dotted line marks the innermost stable circular orbit radius (r_{ms}) for the maximum spin value, which is the smallest r_{ms} among all spin values for a given l and α . Note that, in panels (a) and (i), this minimum $r_{ms} \sim 1$. The hairy Kerr BH differs significantly from the Kerr BH when $l \leq e^{-2}$ and α is close to α_{crit} (panels (b), (c), (e), and (f)) when f_ϕ exhibits a maxima close to the BH and eventually drops to zero. However, such a maxima occurs inside the r_{ms} , which marks the last stable circular orbit. Hence, as long as we confine ourselves to $r \gtrsim r_{ms}$, the behavior of f_ϕ is similar to the Kerr case. For $l \leq e^{-2}$ a clear departure from the Kerr behavior is observed in the magnitude of f_ϕ . For such values of l and when α is close to α_{crit} , the hairy Kerr BH exhibits much smaller f_ϕ than the corresponding Kerr BH with similar spin. Note however, that for such values of l and α , a_{max} is much smaller than a_{max} of the corresponding Kerr BH which is ~ 1 (see Sec. 2). The Kerr-like behavior of f_ϕ is restored for a given l as α approaches α_{max} . We further note from panels (b)-(c) and (e)-(f) of Fig. 5 that for a fixed l and a , f_ϕ seems to increase with α . This behavior is prevalent near the horizon radius, but for $r \gtrsim r_{ms}$ for a given l and a , f_ϕ does not change with α , which is evident from Fig. 5d and Fig. 5g. For $l > e^{-2}$ and $\alpha < \alpha_{coin}$ (e.g. $l = 0.3$ and $\alpha = 2$ Fig. 5h, see Sec. 2), a can only be as high as a_{sec} which is less than a_{max} . In this case, the values of f_ϕ are lower than in the Kerr spacetime. Since, r_{ms} increases with decreasing spin, r_{ms} of these hairy BHs are generally larger than the r_{ms} of hairy BHs with $l > e^{-2}$ and $\alpha > \alpha_{coin}$ (e.g. $l = 0.3$ and $\alpha = 4$, Fig. 5i) where a can go upto a_{max} . For $l = 0.3, \alpha = 4$, f_ϕ rises almost up to the Kerr case after which it saturates up to $\alpha = 6.66$, which is the maximum value α can attain when $l = 0.3$. For hairy BHs with $l > e^{-2}$, when r is close to r_{ms} (e.g. $r \sim 6$), f_ϕ initially decreases with α , then increases and finally reaches a constant value much before α reaches α_{max} as is evident from Fig. 5j. However, when $r \gtrsim r_{ms} + 3R_g$, for a given l and a , f_ϕ does not change with α .

In Fig. 6, we further examine the variation of f_ϕ with r for fixed α but varying l for different choices of spin. Each row corresponds to a fixed value of α , increasing from top to bottom, while l is varied. In Fig. 6a and Fig. 6b we fix the deformation parameter to $\alpha = 0.5$ and consider $l = 1$ and $l = 2$ respectively. Similarly, in Fig. 6d and Fig. 6e the deformation parameter is fixed to $\alpha = 2$ and l is varied to 0.3 and 0.6 respectively. We note from Sec. 2 that whether we fix α to 0.5 or 2, $l_{min} > 0.2$ (see Fig. 1b). Also, for such values of α and lower l values, the spin can go only as high as a_{sec} . The same holds for $\alpha = 6$, $l = 0.15$ (Fig. 6g). Thus, for hairy BHs with $\alpha = 0.5$ & $l = 1$, $\alpha = 2$ & $l = 0.3$, or $\alpha = 6$ & $l = 0.15$, the r_{ms} values are larger than their corresponding hairy counterparts with same α but larger l . The r_{ms} values of the hairy Kerr BH with

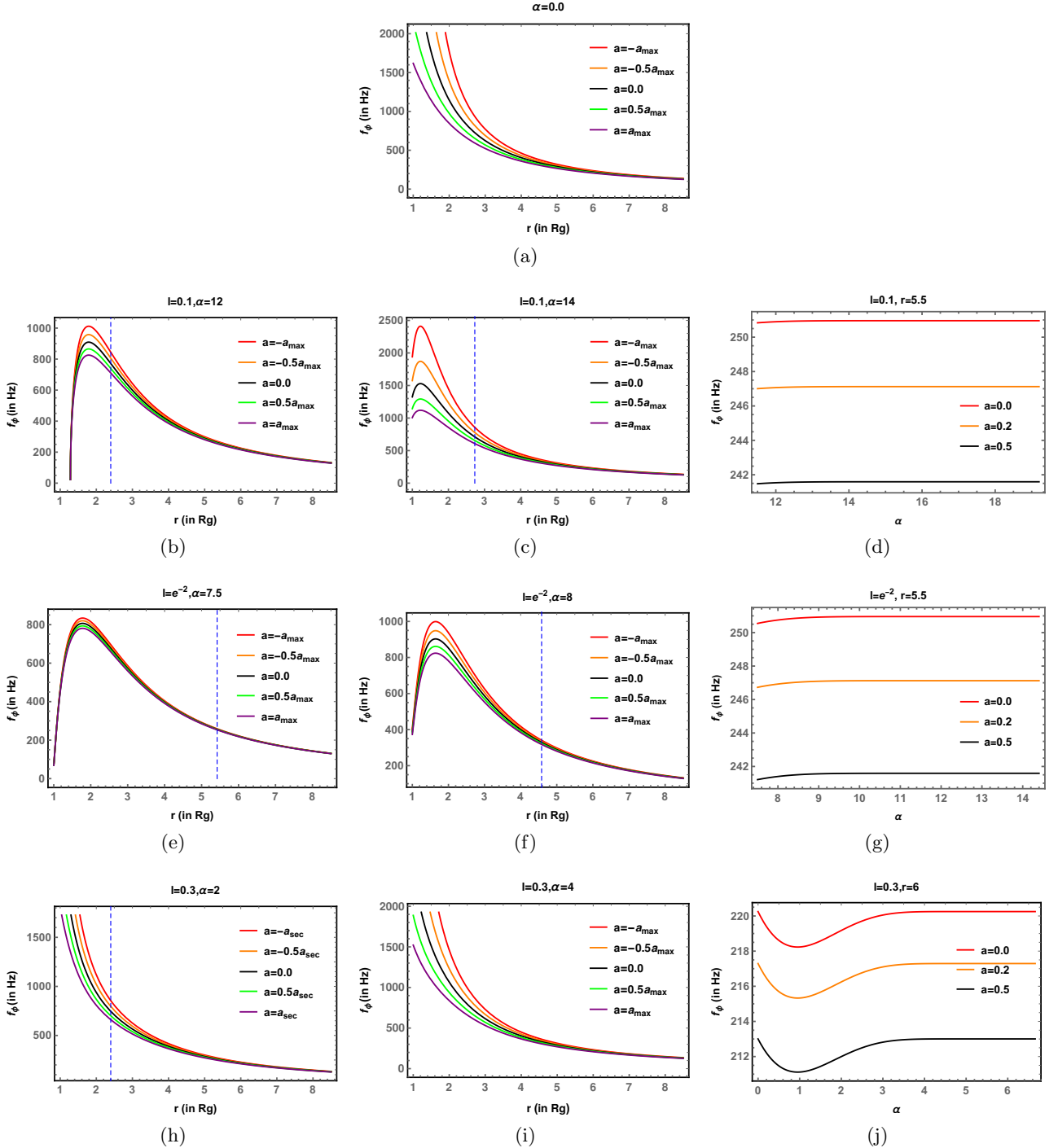


Figure 5: The above figures show the variation of f_ϕ (a) with r for $\alpha = 0$ (Kerr scenario), (b) with r for $l = 0.1, \alpha = 12$, and (c) with r for $l = 0.1, \alpha = 14$, (d) with α for $l = 0.1, r = 5.5$, (e) with r for $l = e^{-2}, \alpha = 7.5$, (f) with r for $l = e^{-2}, \alpha = 8$, (g) with α for $l = e^{-2}, r = 5.5$, (h) with r for $l = 0.3, \alpha = 2$, (i) with r for $l = 0.3, \alpha = 4$, (j) with α for $l = 0.3, r = 6$. In each case we have considered variation with respect to spins from $-a_{max}$ to a_{max} . The above figure is plotted for a $M = 10M_\odot$ BH.

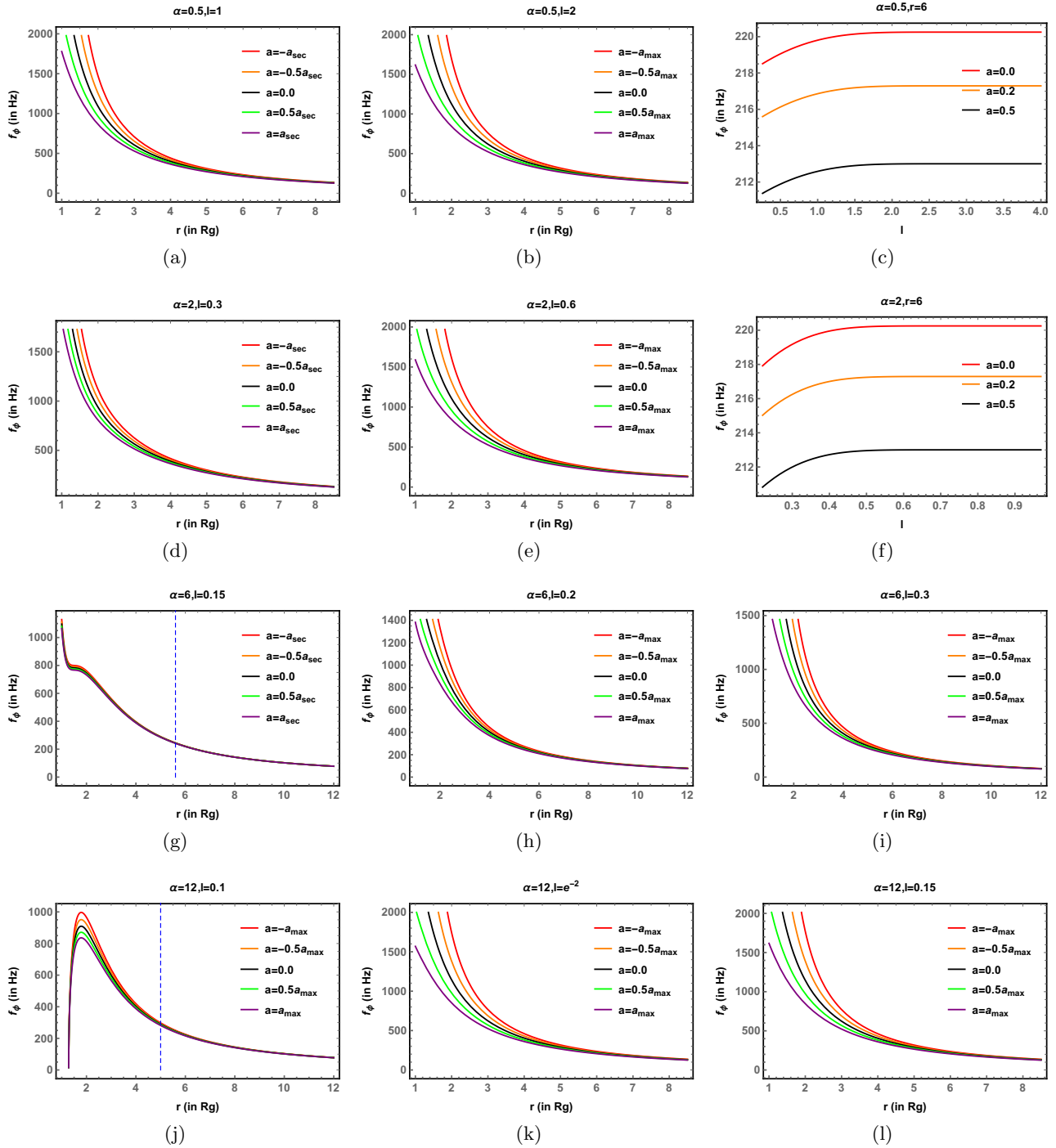


Figure 6: The above figures show the variation of f_ϕ (a) with r , for $\alpha = 0.5, l = 1$, (b) with r , for $\alpha = 0.5, l = 2$, (c) with l , for $\alpha = 0.5$ at $r = 6$, (d) with r , for $\alpha = 2, l = 0.3$, (e) with r , for $\alpha = 2, l = 0.6$, (f) with l , for $\alpha = 2$, at $r = 6$, (g) with r , for $\alpha = 6, l = 0.15$, (h) with r , for $\alpha = 6, l = 0.2$, (i) with r , for $\alpha = 6, l = 0.3$, (j) with r , for $\alpha = 12, l = 0.1$, (k) with r , for $\alpha = 12, l = e^{-2}$, (l) with r , for $\alpha = 12, l = 0.15$. In each case we have considered variation with respect to spins from $-a_{max}$ to a_{max} . The above figures are made for a $M = 10M_\odot$ BH.

maximum achievable prograde spin (which is also the smallest r_{ms}) is represented by the blue dashed line in [Fig. 6](#). For [Fig. 6b](#), [Fig. 6e](#), [Fig. 6h](#) and [Fig. 6k](#), the smallest $r_{ms} \sim 1$. Thus, it is clear from [Fig. 6](#) that for a fixed α and a , f_ϕ seems to increase with l . But this happens for lower l values and as long as $r \sim r_{ms}$. As l increases beyond a certain threshold value upto l_{max} , even near r_{ms} , f_ϕ ceases to exhibit variation with respect to l ([Fig. 6c](#) and [Fig. 6f](#)). This feature is prevalent also for $\alpha \sim 12$, where however $l_{max} \approx 0.167$. Once again for a given α , as l approaches l_{max} , the Kerr features are recovered ([Fig. 5a](#)). Overall, from [Fig. 5](#) and [Fig. 6](#) we note that the hairy Kerr BH which satisfies the SEC has lower f_ϕ compared to the Kerr BH and f_ϕ approaches the Kerr limit either as $\alpha \rightarrow 0$ or $l\alpha \rightarrow 2$.

To get the epicyclic frequencies, we have to perturb the stable circular equatorial orbit both radially and vertically. We can show the perturbation by the following equations

$$r(t) = r_c + \delta r; \quad \delta r \sim e^{i\omega_r t}; \quad \delta r \ll r, \quad (3.10)$$

$$\theta(t) = \frac{\pi}{2} + \delta\theta; \quad \delta\theta \sim e^{i\omega_\theta t}; \quad \delta\theta \ll \frac{\pi}{2}. \quad (3.11)$$

As a first approximation, we assume the two oscillations to be decoupled. From (3.7), we get

$$-g_{rr}(u^0 2\pi f_r \delta r)^2 - g_{\theta\theta}(u^0 2\pi f_\theta)^2 + E^2 \left[U(r_c, \frac{\pi}{2}) + \frac{1}{2} \frac{\partial^2 U}{\partial r^2}(r_c, \frac{\pi}{2}) \delta r^2 + \frac{1}{2} \frac{\partial^2 U}{\partial \theta^2}(r_c, \frac{\pi}{2}) \delta\theta^2 \right] = 0. \quad (3.12)$$

Equating the coefficients of δr^2 and $\delta\theta^2$ to zero, we get the epicyclic frequencies as follows

$$f_r^2 = \frac{c^6}{G^2 M^2} \left[\frac{(g_{tt} + g_{t\phi}\Omega)^2}{2(2\pi)^2 g_{rr}} \left(\frac{\partial^2 U}{\partial r^2} \right)_{r_c, \frac{\pi}{2}} \right], \quad (3.13)$$

$$f_\theta^2 = \frac{c^6}{G^2 M^2} \left[\frac{(g_{tt} + g_{t\phi}\Omega)^2}{2(2\pi)^2 g_{\theta\theta}} \left(\frac{\partial^2 U}{\partial \theta^2} \right)_{r_c, \frac{\pi}{2}} \right], \quad (3.14)$$

where the factor $\frac{c^6}{G^2 M^2}$ is used in order to match the dimension of frequency squared.

In Fig. 7, we have shown the variation of f_r with r , keeping the length parameter l fixed and varying the deformation parameter α and the spin in the allowed range. Fig. 7a corresponds to the Kerr case as when $\alpha = 0$, the metric reduces to Kerr metric, which is provided for comparison purposes. From the figure we note that similar to the Kerr scenario, f_r increases with decreasing distance from the BH, attains a maximum, and then drops to zero at the r_{ms} . For a given α and l , f_r increases with spin and is maximum for prograde maximum spin ($+a_{max}$) and minimum for retrograde maximum spin ($-a_{max}$), as observed in the Kerr BH. In Fig. 7b, Fig. 7c and Fig. 7d we have fixed the length parameter l to 0.1 and varied deformation parameter α to 12, 14, 16 respectively. For all these α values, f_r are less compared to the Kerr case but increase with increasing α and would resemble the Kerr case for maximal α . The same holds true for $l = e^{-2}$ (Fig. 7e, Fig. 7f, and Fig. 7g). In Fig. 7h, Fig. 7i, and Fig. 7j, we have fixed l to 0.3 and varied α to 2, 4 and 6 respectively. In case of $\alpha = 2$, the spin value can rise up to a_{sec} , beyond which the strong energy condition is not satisfied. For $\alpha = 2$, f_r values decrease from Kerr case but for $\alpha = 4$, it rises up and eventually it will saturate to the Kerr case for maximal α . From Fig. 7, we note that for a given l , f_r increases with α as the spin becomes closer to a_{max} , for lower spin, f_r is not that much sensitive to α .

In Fig. 8, we have shown the variation of f_r with r , keeping the deformation parameter α fixed and varying the length parameter l in the allowed spin range. In Fig. 8a and Fig. 8b, we have fixed α value to 0.5 and varied l values to 1 and 2. For lower spins and near the r_{ms} , f_r decreases with l and eventually saturates at higher l (Fig. 8c). From Fig. 8d-Fig. 8f and Fig. 8g-Fig. 8i, f_r seems to increase with increase in l for a fixed α . For $l = 1$, the spin can be as high as a_{sec} and f_r is lower than the Kerr case. Thus, the maximum achievable f_r outside r_{ms} is higher for hairy BHs with a fixed α but larger l . This may be attributed to the increase in a_{max} as l approaches $l_{max} = 2/\alpha$ for a given α . With increasing l and as $l \rightarrow 2/\alpha$ the Kerr scenario is recovered. From Fig. 7 and Fig. 8 we note that in general, the hairy Kerr BH with non-trivial α, l and satisfying the SEC has lower values of radial epicyclic frequency as compared to the Kerr case.

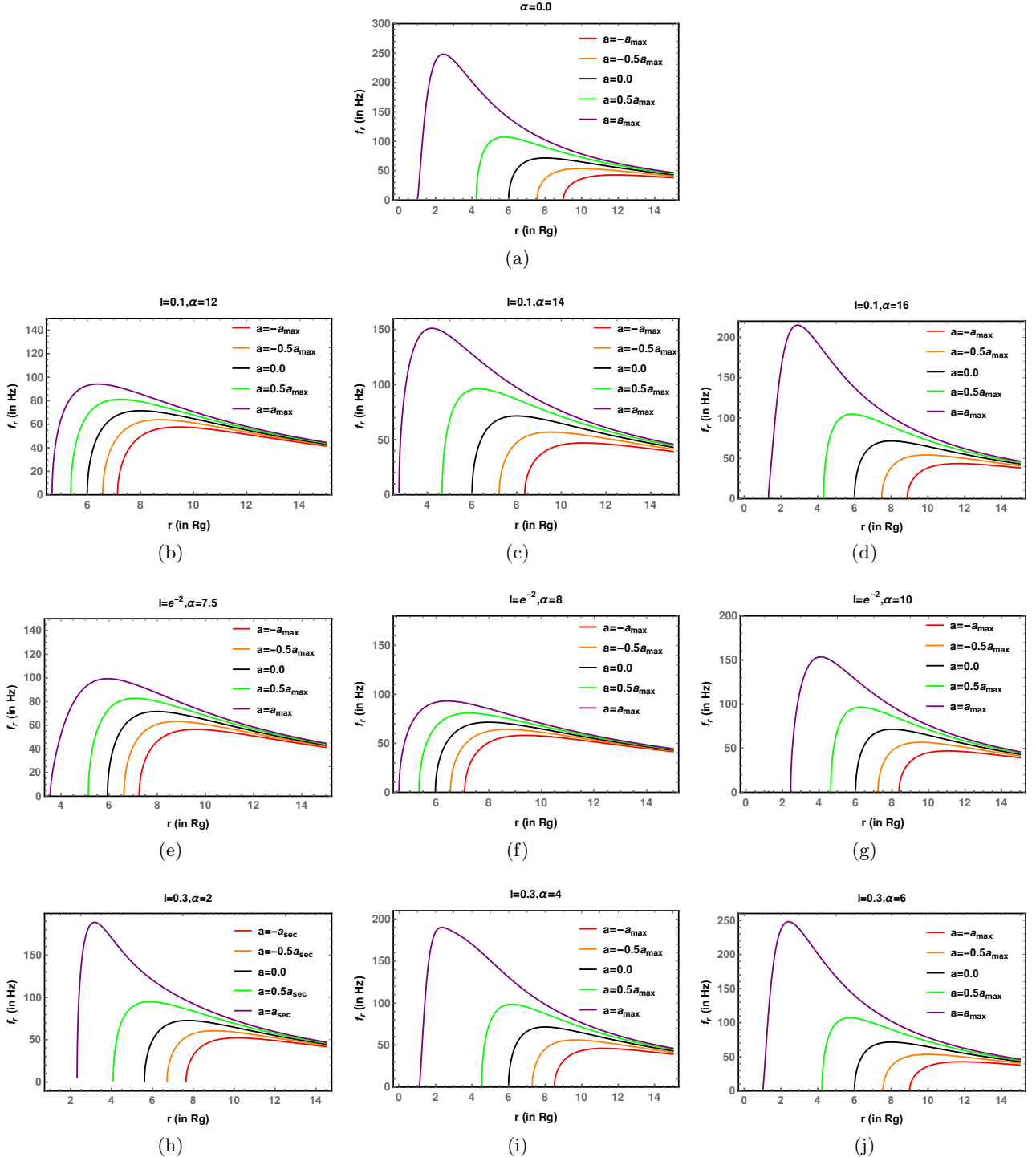


Figure 7: The above figures show the radial variation of f_r for (a) $\alpha = 0$ (Kerr scenario), (b) $l = 0.1, \alpha = 12$, (c) $l = 0.1, \alpha = 14$, (d) $l = 0.1, \alpha = 16$, (e) $l = e^{-2}, \alpha = 7.5$, (f) $l = e^{-2}, \alpha = 8$, (g) $l = e^{-2}, \alpha = 10$, (h) $l = 0.3, \alpha = 2$, (i) $l = 0.3, \alpha = 4$, and (j) $l = 0.3, \alpha = 6$. In each subfigure, we have shown variation with respect to spins in the entire allowed range. The above plot is made for a $M = 10M_\odot$ BH.

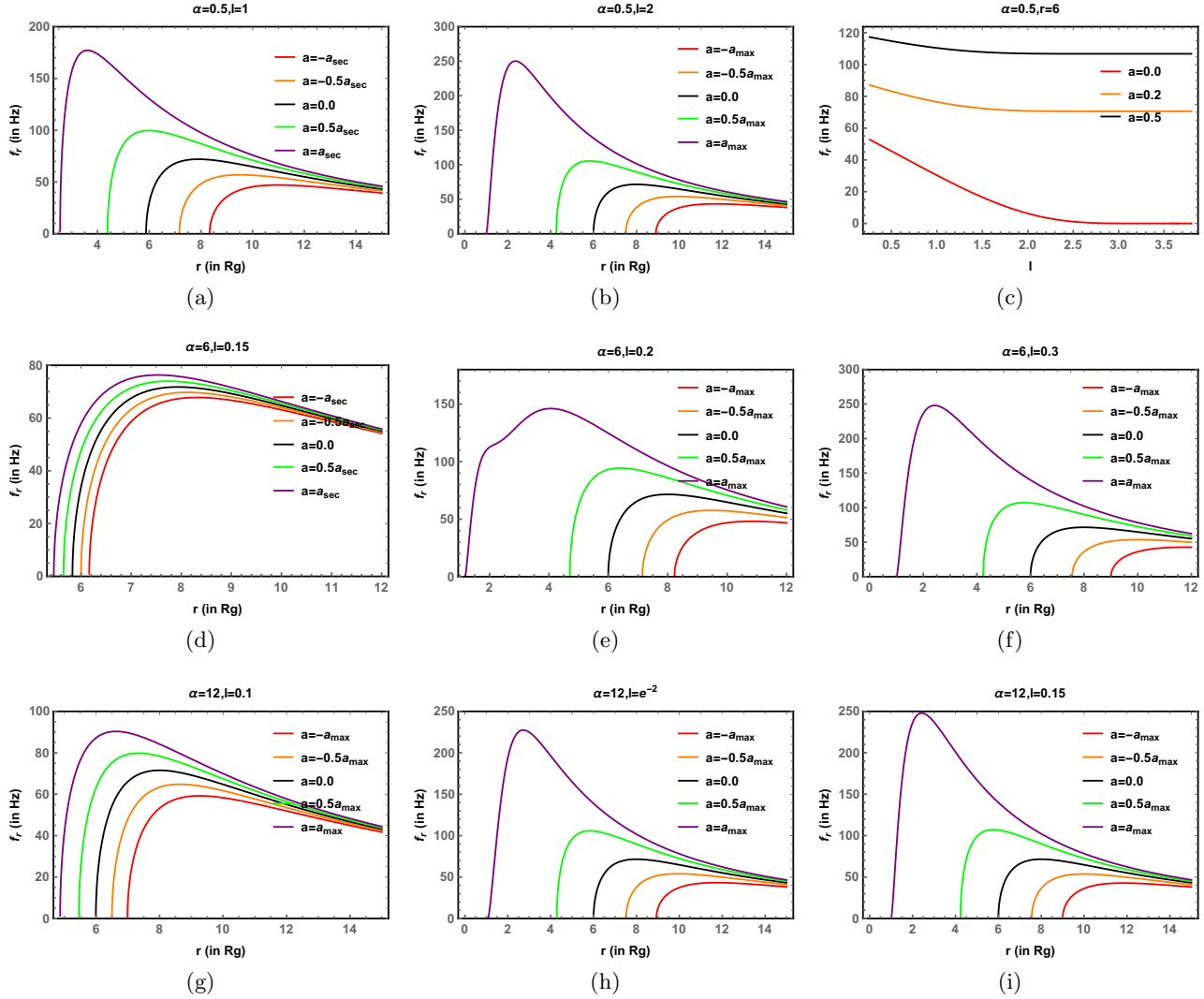


Figure 8: The above figures show the variation of f_r (a) with r , for $\alpha = 0.5, l = 1$, (b) with r , for $\alpha = 0.5, l = 2$, (c) with l , for $\alpha = 0.5$ at $r = 6$, (d) with r , for $\alpha = 6, l = 0.15$, (e) with r , for $\alpha = 6, l = 0.2$, (f) with r , for $\alpha = 6, l = 0.3$, (g) with r , for $\alpha = 12, l = 0.1$, (h) with r , for $\alpha = 12, l = e^{-2}$, (i) with r , for $\alpha = 12, l = 0.15$, for different spins of a $M = 10M_\odot$ BH.

Finally in [Fig. 9](#) we have shown the variation of f_θ with r , keeping the length parameter l fixed and varying the deformation parameter α in the allowed spin range. Here [Fig. 9a](#) corresponds to the Kerr case where $a_{max} \sim 1$ is the maximum spin that the Kerr black hole can attain. We have shown the variation of f_θ for $a = -a_{max}$, $a = -0.5a_{max}$, $a = 0$, $a = 0.5a_{max}$, $a = a_{max}$. We note that f_θ monotonically increases with decreasing radial distance from the BH for the Schwarzschild BH or retrograde spins while for intermediate to maximal prograde spins f_θ attains a maximum and then drops to zero inside the r_{ms} . Hence for $r > r_{ms}$, f_θ is monotonically increasing with decreasing r . Also, f_θ decreases with an increase in spin of the BH.

In [Fig. 9b](#)-[Fig. 9d](#), we fix the length parameter l to 0.1; in [Fig. 9e](#)-[Fig. 9g](#), we fix l to $l = e^{-2}$; and in [Fig. 9h](#)-[Fig. 9i](#), we fix $l = 0.3$; while varying α for each chosen value of l . Here the vertical dotted line represents the inner most stable circular orbit radius r_{ms} for the maximum spin value which is the smallest r_{ms} radius compared to other spin values. In case of [Fig. 9d](#) and [Fig. 9i](#), the smallest r_{ms} is almost 1. From [Fig. 9](#), we observe that the behavior of f_θ as a function of r closely resembles the Kerr case. However, for hairy Kerr black holes with nonzero l and α , and satisfying $l\alpha < 2$, the corresponding r_{ms} is larger than that of their Kerr counterparts. This is mainly because the extremal spin a_{max} of hairy Kerr BHs is smaller than that of their extremal Kerr counterparts (see [Sec. 2](#)). As a consequence, for $r > r_{ms}$, the hairy Kerr BHs generally have smaller f_θ compared to Kerr BHs with similar spin. From [Fig. 9](#) it seems that for $r \gtrsim r_{ms}$, f_θ increases with α for a given l and a . This behavior can be better understood from [Fig. 9j](#) where at $r = 6 R_g$ (i.e., near r_{ms}), f_θ first decreases, then increases and finally saturates to a constant value much before $\alpha \sim \alpha_{max}$.

To understand the sensitivity of f_θ on l we consider [Fig. 10](#). Here, we have shown the variation of f_θ with r , keeping the deformation parameter α fixed and varying the length parameter l in the allowed range of spin. We note that for a given l , when $\alpha l < 1$ (e.g. [Fig. 10a](#), [Fig. 10d](#), and [Fig. 10g](#)), the hairy BH has lower f_θ compared to the Kerr case as long as we are outside $r > r_{ms}$, for reasons discussed earlier. But as l increases for a given α , the Kerr scenario is recovered. Moreover, f_θ is almost insensitive to variation with respect to l for a given α (as elucidated in [Fig. 10c](#) and [Fig. 10f](#)). Overall, departure from the Kerr scenario is observed in the behavior of f_θ with r if the particle is in the vicinity of r_{ms} and the hairy BH has $\alpha l < 1$.

We now turn to the kinematic models proposed in the literature to explain the high-frequency QPOs (HFQPOs) observed in black hole and neutron star systems. HFQPOs typically appear in commensurable pairs, and notably, the ratio between the twin-peak HFQPOs is often found to be 3 : 2. In these models, the predicted QPO frequencies are expressed as linear combinations of the three fundamental frequencies, f_r , f_θ , and f_ϕ , introduced earlier. Although most of these frameworks are designed primarily to account for HFQPOs, the Relativistic Precession Model (RPM) uniquely provides a unified mechanism capable of explaining both HFQPOs and low-frequency QPOs (LFQPOs) simultaneously. We investigate the viability of these models and the hairy Kerr BH scenario in explaining the observed HFQPOs in BH sources.

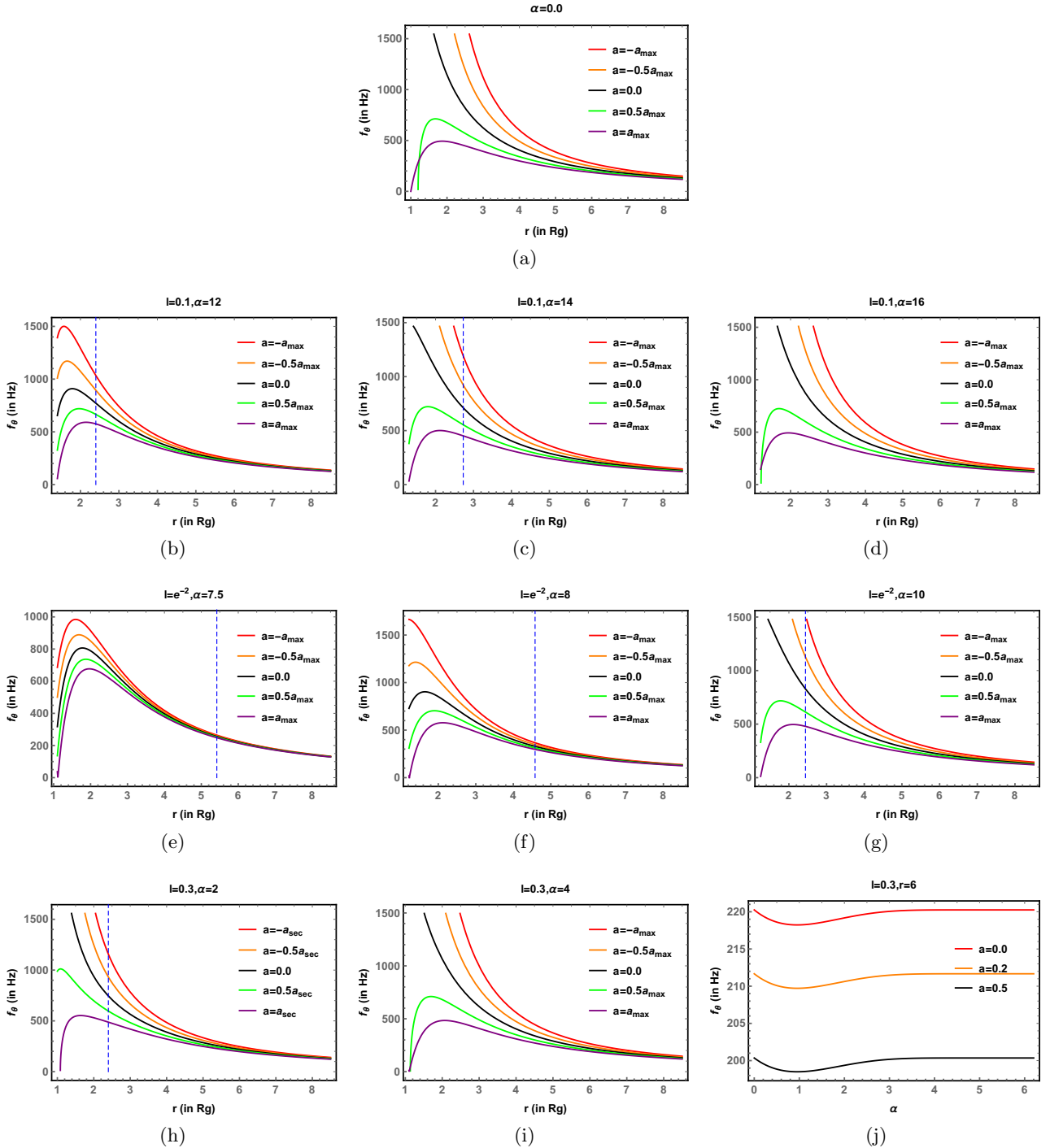


Figure 9: The above figures show the variation of f_θ (a) with r for $\alpha = 0$ (Kerr scenario), (b) with r , for $l = 0.1, \alpha = 12$, and (c) with r , for $l = 0.1, \alpha = 14$, (d) with r for $l = 0.1, \alpha = 16$, (e) with r , for $l = e^{-2}, \alpha = 7.5$, (f) with r , for $l = e^{-2}, \alpha = 8$, (g) with r , for $l = e^{-2}, \alpha = 10$, (h) with r , for $l = 0.3, \alpha = 2$, (i) with r , for $l = 0.3, \alpha = 4$, (j) with α , for $l = 0.3$ at $r = 6$, for different spins of a $M = 10M_\odot$ BH.

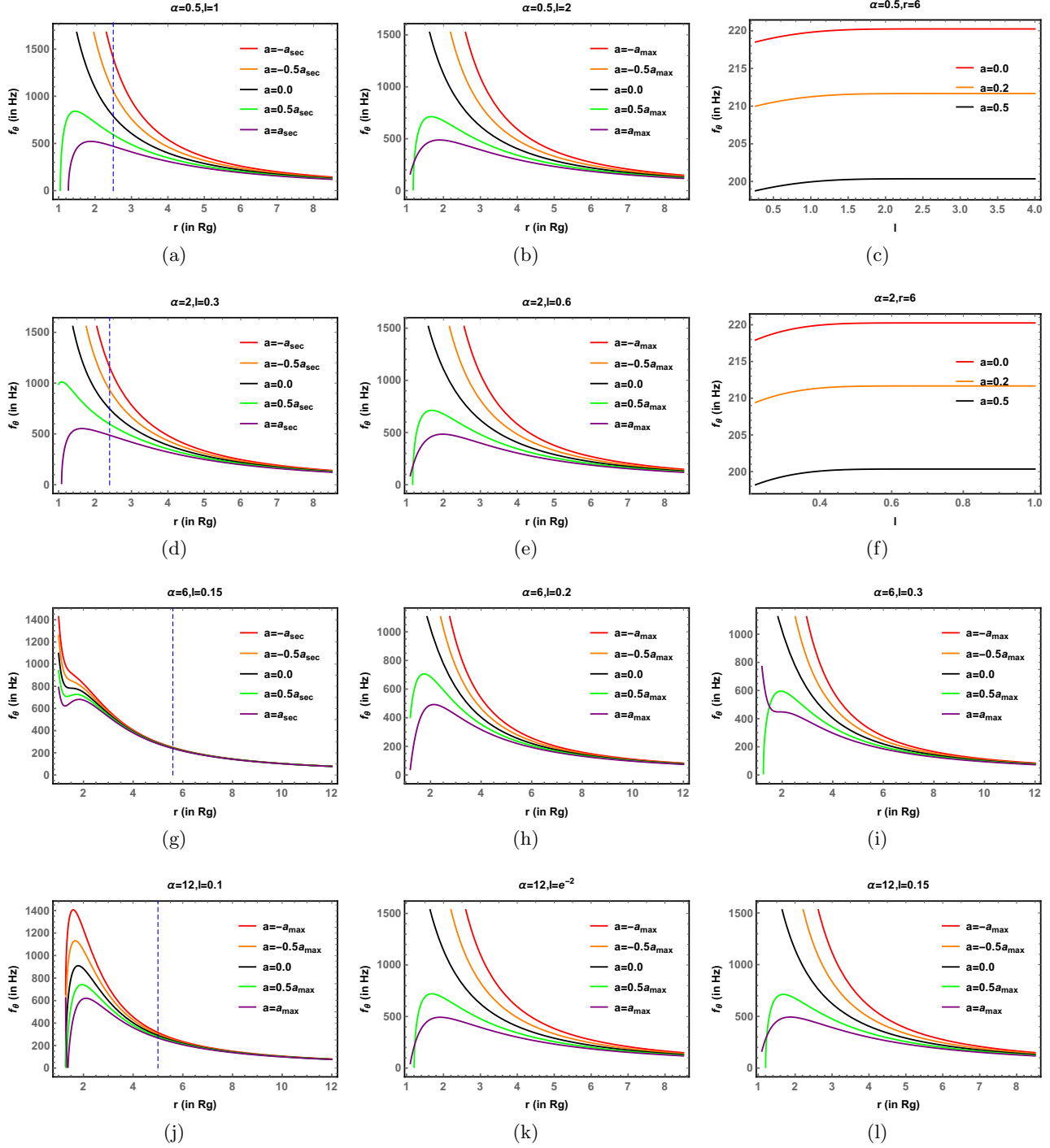


Figure 10: The above figure shows the variation of f_θ (a) with r , for $\alpha = 0.5, l = 1$, (b) with r , for $\alpha = 0.5, l = 2$, (c) with l , for $\alpha = 0.5$ at $r = 6$, (d) with r , for $\alpha = 2, l = 0.3$, (e) with r , for $\alpha = 2, l = 0.6$, (f) with l , for $\alpha = 2$ at $r = 6$, (g) with r , for $\alpha = 6, l = 0.15$, (h) with r , for $\alpha = 6, l = 0.2$, (i) with r , for $\alpha = 6, l = 0.3$, (j) with r , for $\alpha = 12, l = 0.1$, (k) with r , for $\alpha = 12, l = e^{-2}$, (l) with r , for $\alpha = 12, l = 0.15$, for different spins for a $M = 10M_\odot$ BH.

4 Assessment of Model-Predicted HFQPOs in Light of Observational Data

In this section, we compare the HFQPO frequencies predicted by different kinematic models with the corresponding observational measurements. To evaluate how well each model fits the data, we perform an error analysis. The χ^2 minimization technique is employed to quantify the discrepancy between the theoretical estimates and the observed QPO frequencies. Since there are two parameters, l and α , that quantify the deviation of the hairy black holes from the Kerr scenario, the χ^2 function is defined as

$$\chi_i^2(l, \alpha) = \frac{[f_{up1,i} - f_1(l, \alpha, a_{min}, M_{min}, r_{min})]^2}{\sigma_{f_{up1,i}}^2} + \frac{[f_{up2,i} - f_2(l, \alpha, a_{min}, M_{min}, r_{min})]^2}{\sigma_{f_{up2,i}}^2}. \quad (4.1)$$

Source	Mass (M_\odot)	$f_{up1} \pm \Delta f_{up1}$ (Hz)	$f_{up2} \pm \Delta f_{up2}$ (Hz)	$f_{up3} \pm \Delta f_{up3}$ (Hz)
GRO J1655-40	5.4 ± 0.3 [77]	441 ± 2 [78]	298 ± 4 [78]	17.3 ± 0.1 [78]
XTE J1550-564	9.1 ± 0.61 [79]	276 ± 3	184 ± 5	-
GRS 1915+105	$12.4^{+2.0}_{-1.8}$ [80]	168 ± 3	113 ± 5	-
H 1743+322	$8.0 - 14.07$ [81–83]	242 ± 3	166 ± 5	-
Sgr A*	$(3.5 - 4.9) \times 10^6$ [84, 85]	$(1.445 \pm 0.16) \times 10^{-3}$ [63, 86]	$(0.886 \pm 0.04) \times 10^{-3}$ [63, 86]	-
XTE J1859+226	7.85 ± 0.46 [87]	$227.5^{+2.1}_{-2.4}$ [87]	$128.6^{+1.6}_{-1.8}$ [87]	3.65 ± 0.01

Table 1: BH Sources where High-Frequency Quasi-Periodic Oscillations (HFQPOs) are observed.

This expression quantifies the deviation between the model predicted and the observed HFQPO frequencies. Tab. 1 enlists the BH sources which exhibits HFQPOs in their power spectrum. In this context, $f_{up1,i}$ and $f_{up2,i}$ denote the upper and lower HFQPO frequencies for the i -th source, as listed in Tab. 1. The corresponding uncertainties, $\sigma_{f_{up1,i}}$ and $\sigma_{f_{up2,i}}$, represent the observational errors in these measured frequencies, also reported in Tab. 1. The theoretical frequencies f_1 and f_2 for each model are calculated from f_ϕ , f_θ , and f_r following the definitions provided for Relativistic Precession model (RPM) where $f_1 = f_\phi$, $f_2 = f_\phi - f_r$, $f_3 = f_\phi - f_\theta$ and Tidal Disruption model (TDM) where $f_1 = f_\phi + f_r$, $f_2 = f_\phi$.

The steps of our analysis are outlined below:

- First, we choose one of the models between RPM and TDM, in which the frequencies f_1 , f_2 , and, when applicable, f_3 depend on l , α , a , M , and the emission radius r_{cm} associated with the QPO generation.
- We then choose a black hole source from Tab. 1 whose mass range is known, enabling us to compute the theoretical frequencies f_1 , f_2 , and, when applicable, f_3 across that mass interval.
- We fix l and α , with $\alpha l \leq 2$, such that the strong energy condition is satisfied. For this fixed l and α , the spin parameter a is allowed to vary within $-a_{max} \leq a \leq a_{max}$ or $-a_{sec} \leq a \leq a_{sec}$ (see Sec. 2), guaranteeing that the event horizon remains real and positive.
- The black hole mass M is varied within $(M_0 - \Delta M) \leq M \leq (M_0 + \Delta M)$, where M_0 and ΔM denote the central mass and its observational uncertainty as listed in Tab. 1.
- Our main task is to evaluate the frequencies f_1 and f_2 . For each value of M , we allow the emission radius r_{cm} to vary within the range $r_{ms}(a, l, \alpha) \leq r_{cm} \leq r_{ms}(a, l, \alpha) + 20R_g$, where $R_g = GM/c^2$ is the gravitational radius and r_{ms} is the radius of the marginally stable orbit.
- For every combination of M , a , and r_{cm} at the chosen value of l , α , we compute the corresponding χ_i^2 for the selected source. The set of parameters (M, a, r_{cm}) that yields the minimum χ_i^2 provides the best-fit estimates of the mass, spin, and emission radius for that particular l and α . These optimal values are denoted as M_{min} , a_{min} , and $r_{em,min}$ in Eq. 4.1.
- We then repeat this procedure for multiple choices of l , α , allowing us to obtain the variation of χ^2 as a function of l , α for the selected black hole source.
- The same analysis is performed for all black hole sources listed in Tab. 1 for the chosen model.

- Finally, the procedure is repeated for the other model. The minimum value of χ^2 identifies the most favored l, α , together with the corresponding values of M_{\min} and a_{\min} for each black hole source within the framework of that model.

We now provide an overview of the kinematic models proposed to explain HFQPOs observed in the power spectra of certain BHs. By comparing the model predicted frequencies with the observed QPO data, we assess the effectiveness of each model. Tab. 1 lists several BH sources that exhibit HFQPOs, along with their independently measured masses. The characteristic frequencies associated with HFQPOs scale inversely with the mass of the black hole (see Sec. 3). As a result, stellar mass BHs show HFQPOs in the range of a few hundred hertz, whereas supermassive BHs such as Sgr A* produce oscillations in the millihertz range. From Tab. 1, it is clear that HFQPOs often appear as pairs of commensurate frequencies, typically denoted by f_{up1} and f_{up2} , with a characteristic ratio close to 3:2. Since these frequencies correspond to combinations of the three fundamental frequencies (f_r, f_θ, f_ϕ), they depend mainly on the spacetime geometry near the BH and are far less sensitive to the detailed accretion physics. Consequently, HFQPOs provide a relatively clean probe of the underlying metric compared to other observational diagnostics such as the continuum spectrum or the iron line profile.

Kinematic models interpret QPOs as a direct consequence of the motion of matter in the accretion disk around compact objects such as black holes. In these models, the observed frequencies arise purely from the geodesic motion of test particles in curved spacetime, without invoking complicated magnetohydrodynamic or radiative processes within the disk. The oscillations are therefore attributed to fundamental dynamical motions - such as orbital rotation, radial epicyclic oscillations, and vertical epicyclic oscillations - as well as relativistic precession effects induced by strong gravitational fields.

4.1 Relativistic Precession Model

The Relativistic Precession Model (RPM) is one of the most influential kinematic frameworks used to interpret HFQPOs in systems containing compact objects such as black holes and neutron stars. Originally developed to explain the twin-peak HFQPOs observed in neutron star binaries, the model was later extended to black hole sources once similar oscillatory features were detected in their power spectra. In the RPM framework, the observed QPO frequencies are directly associated with the relativistic orbital motion of matter in the inner regions of the accretion disk. The model identifies three fundamental frequencies arising from geodesic motion in strong gravity:

- **Azimuthal (orbital) frequency f_ϕ :** the basic frequency corresponding to circular motion of matter around the compact object.
- **Periastron precession frequency $f_\phi - f_r$:** produced by the relativistic advance of the periastron due to spacetime curvature. This frequency provides a natural explanation for the observed twin HFQPO peaks.
- **Nodal (Lense Thirring) precession frequency $f_\phi - f_\theta$:** arising from the frame-dragging effect induced by the spin of the compact object. This frequency is used to account for low-frequency QPOs such as that observed in GRO J1655-40.

A central assumption of the RPM is that all QPOs originate from the same radial location in the accretion disk, typically close to the innermost stable circular orbit (ISCO). Under this assumption, the three frequencies above provide a self-consistent and physically motivated scheme for interpreting both high- and low-frequency QPOs within a unified model. The strength of this model lies in its ability to connect the observed QPO frequencies to the geometry of the spacetime. Since the model depends only on the metric parameters and the emission radius, it serves as a powerful probe of strong-gravity effects, particularly periastron advance and frame-dragging in the vicinity of compact objects. Now, we discuss our result related to the RPM.

1. GRO J1655-40

In Fig. 11a and Fig. 11b we show the variation of $\ln\chi^2$ with α for different choices of l when the RPM is used to explain the twin-peak HFQPOs and the LFQPO of the source GRO J1655-40. We note that for $\alpha = 0$

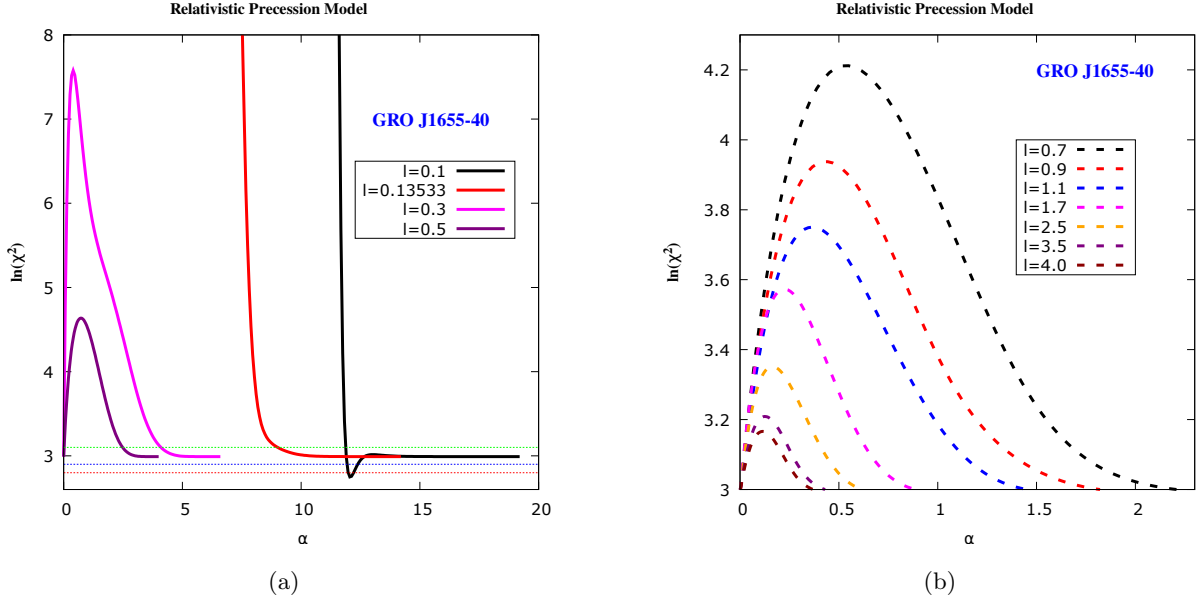


Figure 11: The above figure shows the variation of $\ln\chi^2$ with α for different choices of l when the RPM model is used to explain HFQPOs and LFQPOs of GRO J1655-40. The red, blue, and green dotted lines are associated with the $1-\sigma$, $2-\sigma$, and $3-\sigma$ confidence intervals, which correspond to $\chi^2_{min} + 1$, $\chi^2_{min} + 2.71$, and $\chi^2_{min} + 6.63$ respectively.

and $\alpha = \alpha_{max} = 2/l$, the errors are the same, as both represent the Kerr case. While we have shown only certain values of l in Fig. 11a and Fig. 11b, we have considered $0.1 \leq l \leq 4$ in intervals of 0.2 for our analysis. For each l we have varied α between $\alpha_0 \leq \alpha \leq \alpha_{max} = 2/l$ in intervals of 0.1 when $l \geq 1.7$ and in intervals of 0.2 when $0.1 \leq l < 1.7$. This applies for all the BHs considered here and for both the models. Note that, $\alpha_0 \sim \alpha_{crit}$ for $l < 0.3$ and ~ 0 otherwise (see Sec. 2). We note from Fig. 11 that $\ln\chi^2$ attains a minima near $l \sim 0.1$, $\alpha \sim 12$. The red, blue and green dotted lines are associated with the $1-\sigma$, $2-\sigma$ and $3-\sigma$ confidence intervals, which correspond to $\chi^2_{min} + 1$, $\chi^2_{min} + 2.71$ and $\chi^2_{min} + 6.63$ respectively [88]. It is to be noted that for $l = 0.1$ and $l = e^{-2} \approx 0.13533$, we have not started from $\alpha = 0$ (as shown in Fig. 11a), because SEC is satisfied from $\alpha = \alpha_{crit} \approx 11.4$ (for $l = 0.1$) and $\alpha = \alpha_{crit} \approx 7.4$ (for $l = e^{-2}$) respectively, to $\alpha = \alpha_{max} \approx 2/l$ (see Sec. 2). From Fig. 11a, we notice a sharp decrease in $\ln\chi^2$ for $l = 0.1$ which attains a minima, increases slightly and then saturates. For $l = 0$, SEC is not satisfied for any α , therefore we have excluded this from our consideration. Since $\alpha \sim 0$ and $\alpha l \sim 2$ results in the Kerr metric, the figure reveals that the Kerr scenario is ruled out outside $2-\sigma$ by the RPM model. Although it appears from 11 that GR is allowed within the $3-\sigma$ interval, if we had taken more points near $l \sim 0.1$ $\alpha \sim 12$, then we would have noticed that the magnitude of $\chi^2_{min} \sim 0$, i.e., near $l \sim 0.1$ $\alpha \sim 12$, χ^2 attains a very sharp minima. Thus, even when the $3-\sigma$ interval is considered GR is excluded. Thus, if RPM is used to explain the QPOs of GRO J1655-40, the hairy Kerr BH scenario, particularly with $l \sim 0.1$, $\alpha \sim 12$ seems to be observationally favored compared to the general relativistic scenario. We have further confirmed this by Markov Chain Monte Carlo (MCMC) simulation in the next section.

2. XTE J1550-564

When RPM is used to explain the twin-peak HFQPO data of XTE J1550-564, from Fig. 12, we note that the χ^2 assumes very high values for $l \leq e^{-2}$ and $\alpha \simeq \alpha_{crit}$. Thus, the hairy BH scenario with such values of l , α are ruled out outside $3-\sigma$ for the source XTE J1550-564. Once again, the red, blue and green dotted lines represent the $1-\sigma$, $2-\sigma$, and $3-\sigma$ confidence intervals, respectively, from χ^2_{min} . The χ^2 does not attain a sharp minima for any particular l, α , but is generally ~ 0 for most choices of l, α except the ones mentioned above. Thus, the HFQPO data of XTE J1550-564 cannot distinguish the Kerr scenario from the hairy-Kerr scenario with $l > e^{-2}$ or $l \leq e^{-2}$ but $\alpha > \alpha_{crit}$.

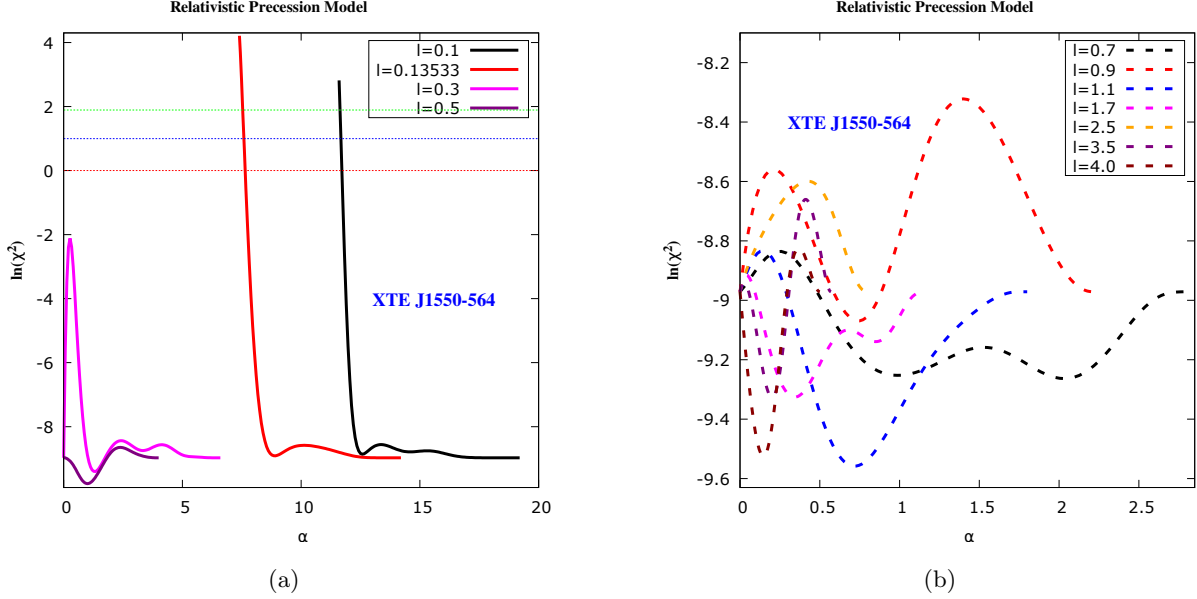


Figure 12: The above figure shows the variation of $\ln\chi^2$ with α for different choices of l when the RPM model is used to explain the HFQPOs of XTE J1550-564

3. GRS 1915+105 & H 1743+322

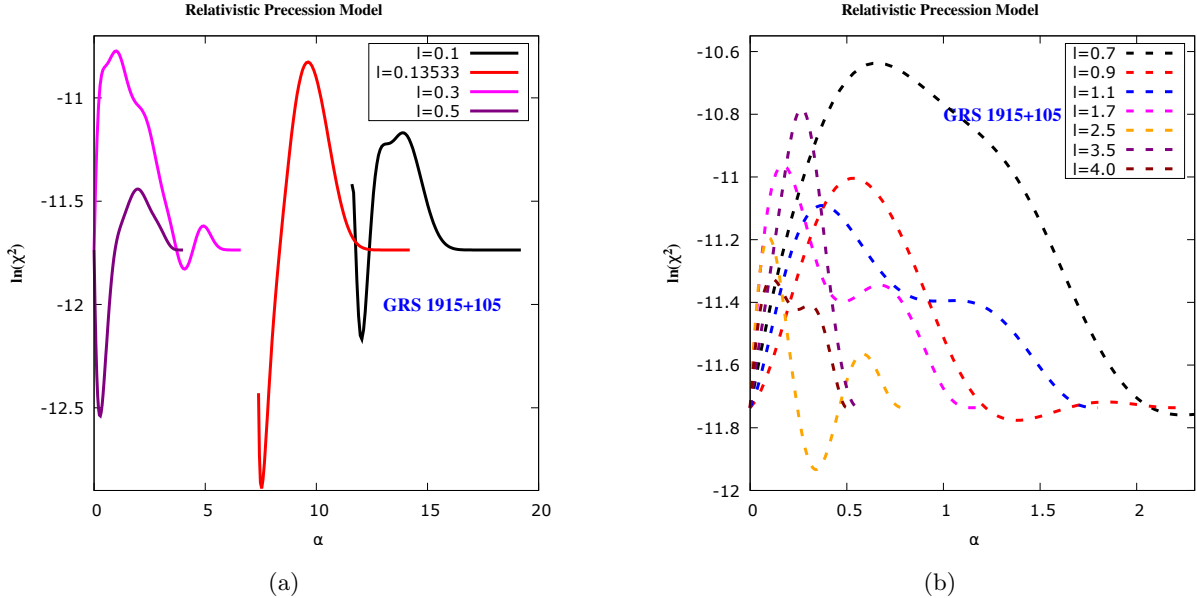


Figure 13: The above figure shows the variation of $\ln\chi^2$ with α for different choices of l when the RPM model is used to explain the HFQPOs of GRS 1915+105.

When RPM is used to explain the twin-peak HFQPO data of GRS 1915+105 and H 1743+322, from Fig. 13 and Fig. 14, we note that $\chi^2 \sim 0$ for all allowed values of l, α . Once again the errors remain essentially the same at $\alpha = 0$ and $\alpha = \alpha_{\max}$, with only minor variations occurring in the intermediate region. These variations are very weakly sensitive to l, α , and therefore do not significantly constrain the parameter space. Thus the HFQPO data of GRS 1915+105 and H 1743-322 fail to differentiate between the Kerr and the hairy Kerr scenario.

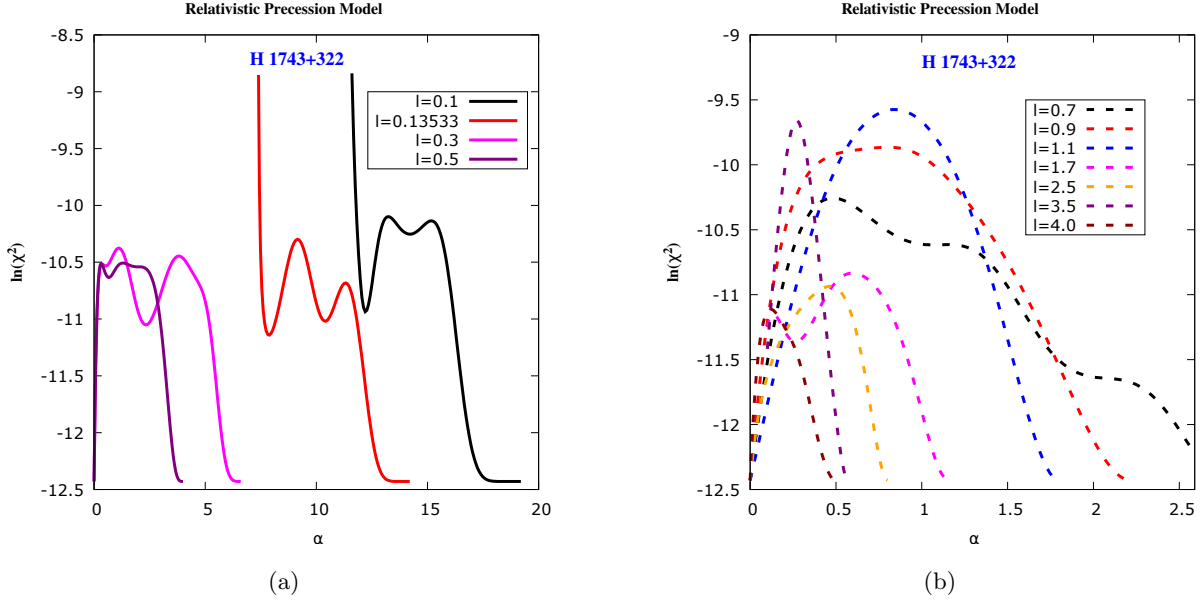


Figure 14: The above figure shows the variation of $\ln\chi^2$ with α for different choices of l when the RPM model is used to explain the HFQPOs of H 1743-322

4. Sgr A*

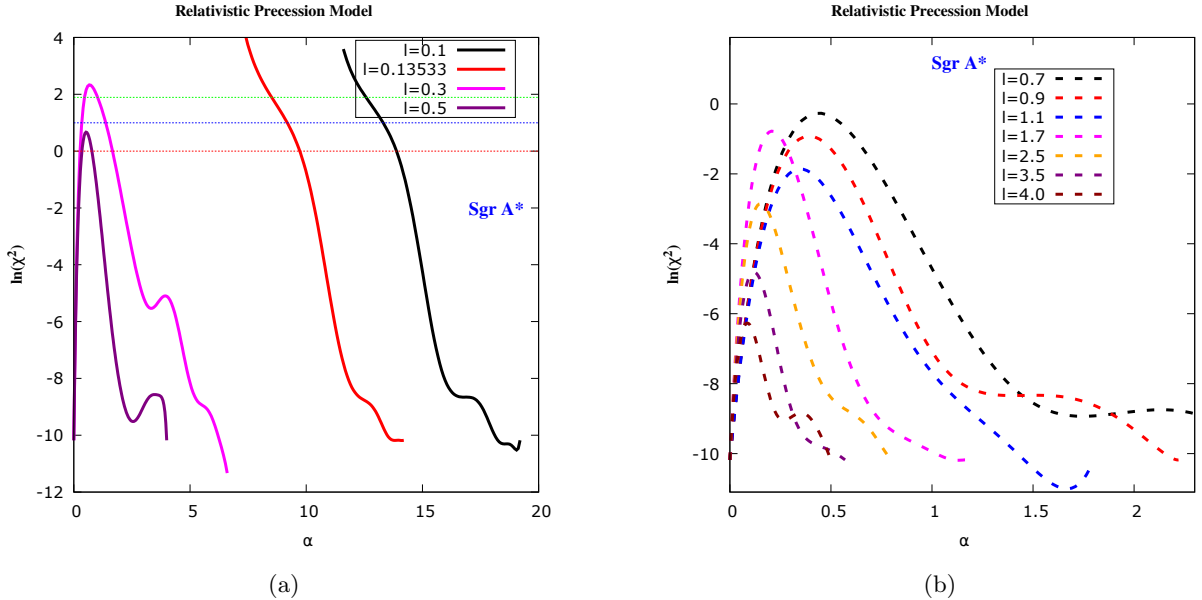


Figure 15: The above figure shows the variation of $\ln\chi^2$ with α for different choices of l when the RPM model is used to explain the HFQPOs of Sgr A*. The red, blue and green dotted lines are associated with the $1-\sigma$, $2-\sigma$ and $3-\sigma$ confidence intervals, which correspond to $\chi_{min}^2 + 1$, $\chi_{min}^2 + 2.71$ and $\chi_{min}^2 + 6.63$ respectively. Here $\chi_{min} \sim 0$.

Next, we discuss our result for supermassive BH Sgr A*. From Fig. 15a and Fig. 15b we note that $\chi_{min}^2 \sim 0$. For $l \lesssim e^{-2}$, α close to α_{crit} are ruled out outside $3-\sigma$ (green dotted line in Fig. 15). For $l \sim e^{-2}$ and $l \sim 0.1$, the allowed range of α within $1-\sigma$ corresponds to $10 \lesssim \alpha \lesssim \alpha_{max} = 2/l$ and $15 \lesssim \alpha \lesssim \alpha_{max} = 2/l$, respectively. For $0.3 \lesssim l \lesssim 0.5$, intermediate values of α are observationally less favored compared to $\alpha \rightarrow 0$ or $\alpha \rightarrow \alpha_{max}$ (Fig. 15a). For $l \gtrsim 0.7$, all values of α between $0 \lesssim \alpha \lesssim \alpha_{max}$ are allowed within $1-\sigma$. Thus, in the context of the RPM model, the HFQPO data of Sgr A* are best described either by the Kerr model or by a hairy

Kerr model with relatively large length parameter ($l \gtrsim 0.7$ for any allowed α), or alternatively with smaller l provided the combined deformation satisfies $\alpha l \gtrsim 1$.

5. XTE J1859+226

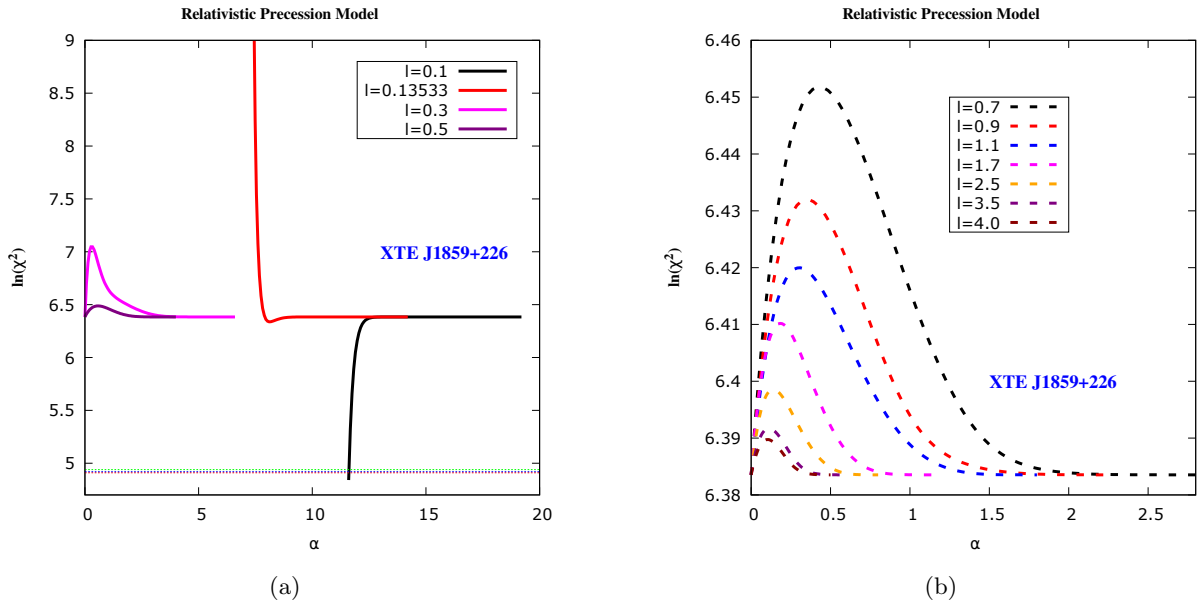


Figure 16: The above figure shows the variation of $\ln\chi^2$ with α for different choices of l when the RPM model is used to explain the HFQPO data of XTE J1859+226. The red, blue and green dotted lines are associated with the $1-\sigma$, $2-\sigma$ and $3-\sigma$ confidence intervals, which correspond to $\chi^2_{min} + 1$, $\chi^2_{min} + 2.71$ and $\chi^2_{min} + 6.63$ respectively. Since the variation of χ^2 with respect to α is substantial, the 3 confidence contours seem to overlap when plotted in the log scale.

Now, we discuss our result related to XTE J1859+226 BH. For $l \geq 0.3$, χ^2 assumes the same value for $\alpha \rightarrow 0$ or $\alpha \rightarrow \alpha_{max}$ as both represent the Kerr case. From Fig. 16a we note that χ^2 attains a global minimum at $l \simeq 0.1$ and $\alpha \simeq \alpha_{crit} \approx 12$. Even the Kerr scenario is ruled out outside $3-\sigma$ if RPM is used to explain the QPO data of XTE J1859+226. For this black hole, the hairy BH scenario is more favored, the parameter space is highly constrained and we will confirm this global minima by MCMC in the next section.

Therefore, considering the RPM model, GRO J1655-40 and XTE J1859-226 seem to favor the hairy Kerr scenario with $l \sim 0.1$ and $\alpha \sim 12$. For XTE J1550-564 and Sgr A*, lower l with $0 < \alpha l \lesssim 1$ are ruled out, while for GRS 1915+105 and H 1743+322 the HFQPO data cannot distinguish the Kerr and the hairy Kerr scenario.

4.1.1 Parameter Constraints from MCMC Analysis

In our earlier analysis, the model parameters were determined through a direct grid based search. In that approach, we scanned over the allowed ranges of the length parameter l , deformation parameter α , the spin a , the black hole mass M , and the emission radius r_{cm} , computing the corresponding χ^2 for every point in the grid. The set of parameters yielding the lowest value of χ^2 was taken as the best fit. A crucial requirement for this technique is that the grid must be fine enough to ensure that the global minimum is not overlooked. To confirm that our grid resolution is adequate, we compare these results with those from a Bayesian inference scheme that uses Markov Chain Monte Carlo (MCMC) sampling.

The posterior probability distribution for the parameter vector $\theta \equiv \{l, \alpha, a, M, r_{cm}\}$ is written as

$$P(\theta|D) = \frac{P(D|\theta)P(\theta)}{P(D)} \quad (4.2)$$

where $P(\theta)$ is the prior on the parameters, $P(D|\theta)$ corresponds to the likelihood, and $P(D)$ is the evidence, which can be taken as unity since the data set is fixed [89]. For the parameters l , α , a , and r_{cm} , we adopt uniform

priors across their allowed domains. For the mass parameter M , we choose Gaussian priors for GRO J1655–40 and XTE J1859+226, considering earlier independent measurements (Tab. 1). As we could strongly constrain the parameter space for GRO J1655-40 and XTE J1859+226 from the grid search, here we present the corner plots for only these two black holes. The likelihood incorporates the contributions from the upper and lower HFQPOs and, where relevant, the LFQPO as well – for example, GRO J1655-40 displays a pair of HFQPOs along with a LFQPO, all of which are accounted for within the RPM framework. This likelihood is given as,

$$\log \mathcal{L} = \log \mathcal{L}_{U_1} + \log \mathcal{L}_{U_2} + \log \mathcal{L}_L, \quad (4.3)$$

where

$$\log \mathcal{L}_{U_1} = -\frac{1}{2} \frac{\{f_{\text{up}1,i} - f_1(l, \alpha, a, M, r_{\text{em}})\}^2}{\sigma_{\text{up}1,i}^2}, \quad (4.4)$$

$$\log \mathcal{L}_{U_2} = -\frac{1}{2} \frac{\{f_{\text{up}2,i} - f_2(l, \alpha, a, M, r_{\text{em}})\}^2}{\sigma_{\text{up}2,i}^2}, \quad (4.5)$$

$$\log \mathcal{L}_L = -\frac{1}{2} \frac{\{f_{\text{up}3,i} - f_3(l, \alpha, a, M, r_{\text{em}})\}^2}{\sigma_{\text{up}3,i}^2}. \quad (4.6)$$

From Fig. 17a and Fig. 17b, we confirm that for GRO J1655-40 and XTE J1859+226, the parameter

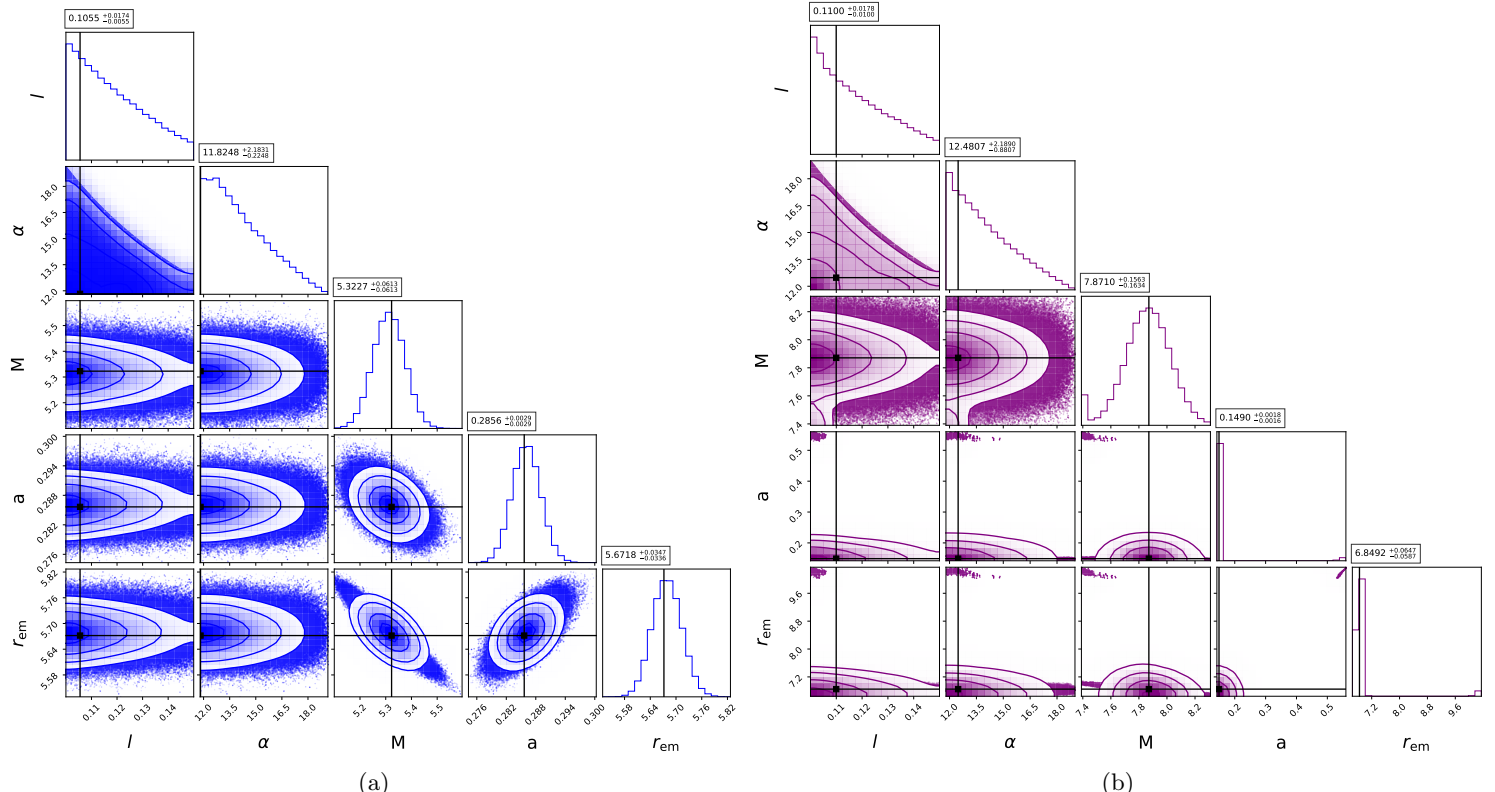


Figure 17: Constraints on the model parameters using the QPO data of GRO J1655-40 (blue) and XTE J1859+226 (magenta) based on RPM model.

estimates based on the grid-search and the MCMC methods are in agreement. However, $\chi_{\text{min}} \sim 0.0146$ for GRO J1655-40 and $\chi_{\text{min}} \sim 0.000618$ for XTE J1859+226.

4.2 Tidal Disruption Model

In the Tidal Disruption Model (TDM), the origin of HFQPOs is attributed to the interaction between the black hole's tidal gravitational field and small, overdense patches of plasma that appear within the accretion disk.

These patches, or clumps, form because the disk is not perfectly uniform, and as they drift inward, the rapidly changing gravitational pull across their extent begins to stretch and tear them apart. During this process the clumps are elongated along their orbit, eventually taking on a ring-like shape. Once this structure forms, it undergoes characteristic oscillations influenced both by the geometry of the spacetime around the black hole and the dynamics of accretion flow.

Within this picture, the higher-frequency QPO is interpreted as the sum of the orbital motion and the radial oscillation of the distorted ring, represented as $f_1 = f_\phi + f_r$. The lower HFQPO corresponds simply to the orbital motion, $f_2 = f_\phi$. Because these frequencies are tied to the black hole mass, spin, charge, and the radius at which the emission originates (r_{cm}), they can in principle be used to infer the properties of the system. As the clumps are disrupted, the infalling material heats up through viscous effects and the release of gravitational binding energy, giving rise to strong X-ray emission. In this way, the model connects the observed HFQPOs with the basic orbital dynamics of matter in the disk and with the tidal forces operating near the black hole.

1. GRO J1655-40, XTE J1550-564, GRS 1915+105 & H 1743-322

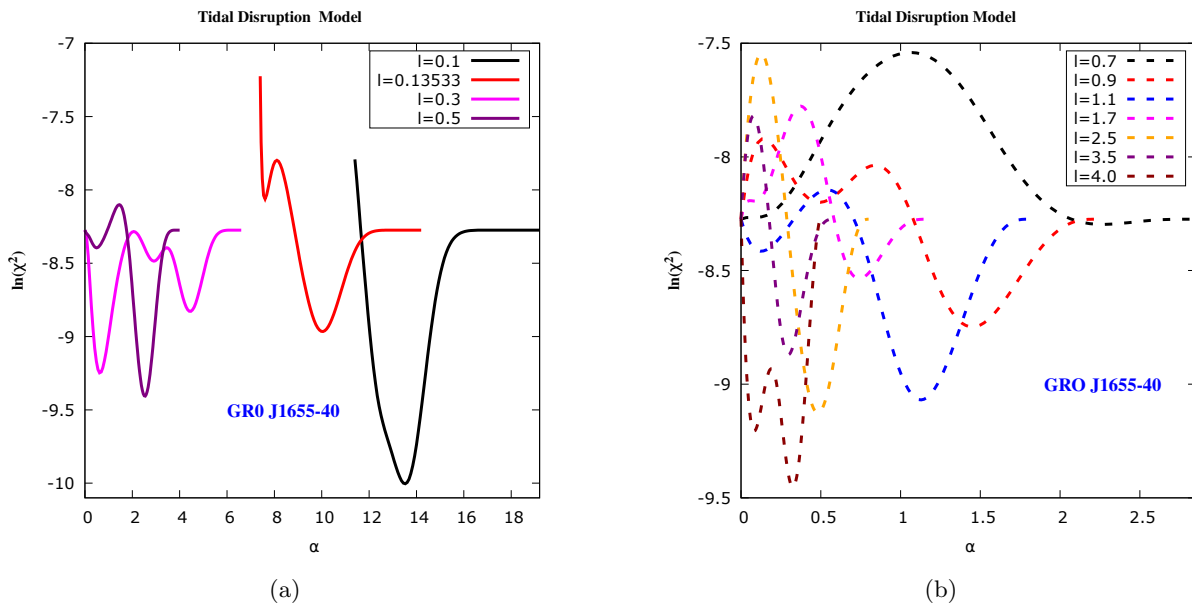


Figure 18: The above figure shows the variation of $\ln\chi^2$ with α for different choices of l when the TDM model is used to explain the HFQPOs of GRO J1655-40

When we compare the observed QPO frequencies of GRO J1655-40 with the TDM model we note that the χ^2 values are nearly zero irrespective of whether we consider the Kerr case or the hairy Kerr scenario. From Fig. 18a, it can be seen that for $l = 0.1$ and $l = 0.13533$, the behaviour of the error shows a non-monotonic trend: as α increases, the error initially declines, but beyond a particular value of α – around $\alpha = 10$ for $l = 0.13533$ and $\alpha = 13.9$ for $l = 0.1$ – the error reverses its trend, rises again, and eventually approaches the value corresponding to the Kerr limit ($\alpha = 0$). For the other choices of l that appear in Fig. 18a and Fig. 18b, the situation is different. In these cases, the errors at $\alpha = 0$ and at $\alpha = \alpha_{\text{max}}$ are practically indistinguishable (since both correspond to the Kerr scenario), and the intermediate values of α produce only minor deviations. The same can be observed for higher values of l in Fig. 18b. Consequently, imposing 1σ , 2σ , or 3σ bounds does not meaningfully restrict the parameter space, as the error curves barely respond to changes in α or l . Similar conclusions can also be achieved for other BH sources like XTE J1550-564, GRS 1915+105, and H 1743-322, which is evident from Fig. 19, Fig. 20 and Fig. 21.

Therefore, the TDM framework does not provide any robust constraints on the hairy parameters for the BH sources GRO J1655-40, XTE J1550-564, GRS 1915+105, and H 1743-322, indicating that the QPO data associated with these BHs cannot distinguish between the Kerr and the hairy Kerr scenario.

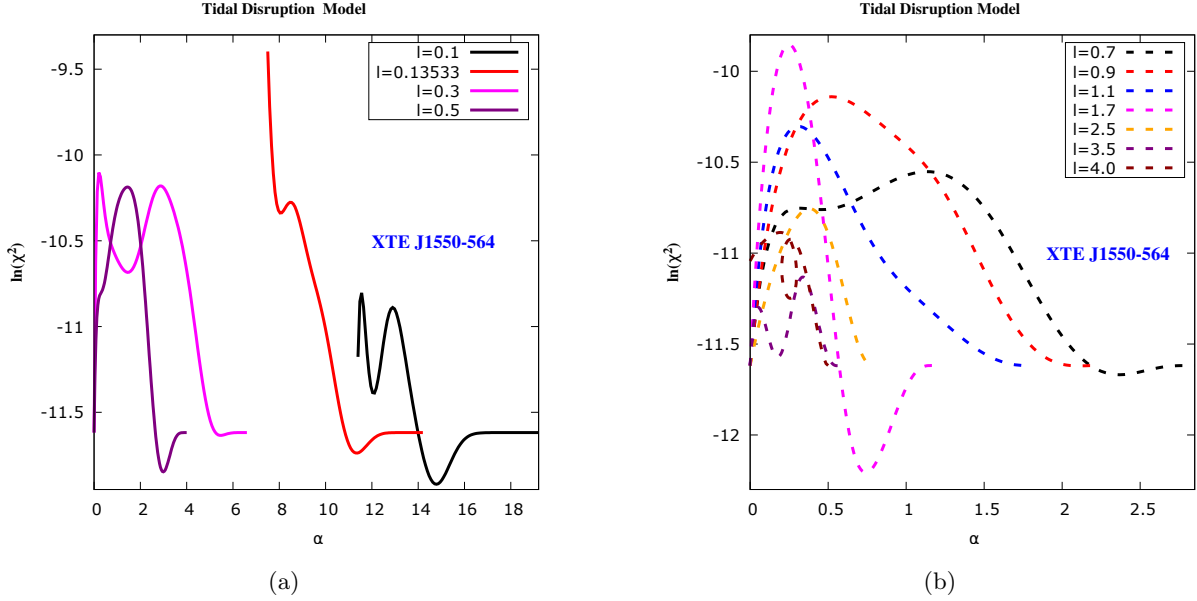


Figure 19: The above figure shows the variation of $\ln\chi^2$ with α for different choices of l when the TDM model is used to explain the HFQPOs of XTE J1550-564

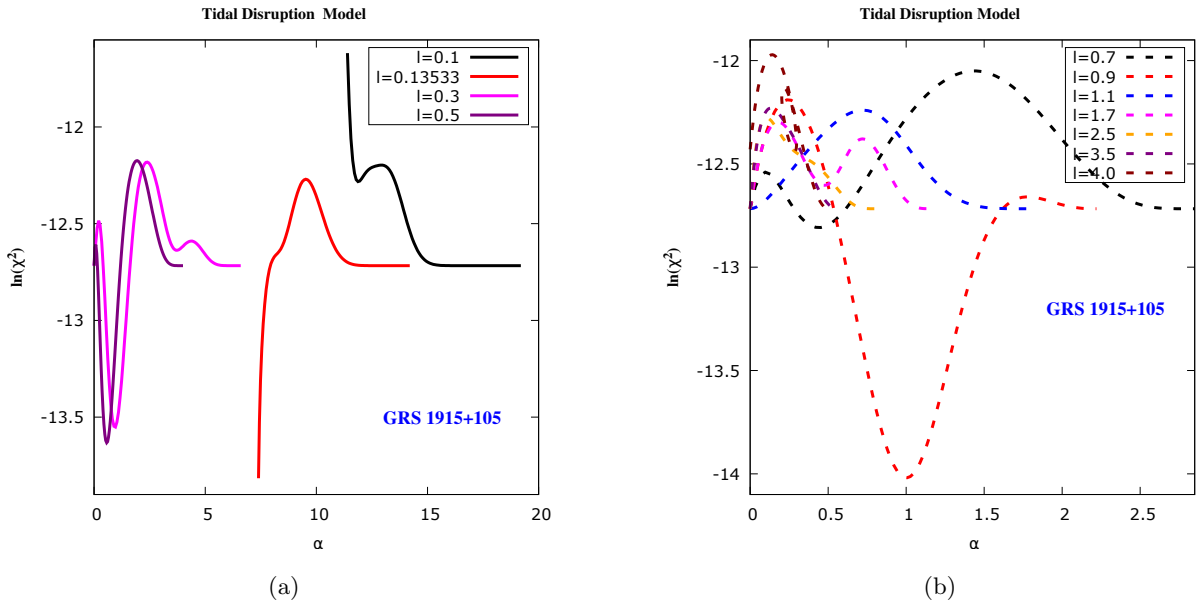


Figure 20: The above figure shows the variation of $\ln\chi^2$ with α for different choices of l when the TDM model is used to explain the HFQPOs of GRS 1915+105.

2. Sgr A*

When TDM is used to fit the HFQPO data of Sgr A*, we note from Fig. 22a that for $l = 0.1$ and $l = e^{-2}$ (i.e., $l \leq e^{-2}$), the χ^2 increases substantially near α_{crit} . Thus, for $l \sim 0.1$, $\alpha_{crit} \lesssim \alpha \lesssim 15$ are ruled out outside $1-\sigma$ while $\alpha_{crit} \lesssim \alpha \lesssim 13$ are ruled out outside $3-\sigma$. Similarly, for $l \sim e^{-2}$, $\alpha_{crit} \lesssim \alpha \lesssim 10$ are ruled out outside $1-\sigma$ while $\alpha_{crit} \lesssim \alpha \lesssim 8$ are ruled out outside $3-\sigma$. For $0.3 \lesssim l \lesssim 0.7$, the Kerr scenario is preferred and the intermediate values of α are ruled out (refer Fig. 22a). For higher values of l (see Fig. 22b), for a given l , the χ^2 maximizes for intermediate α , but the χ^2 values are not high enough, such that all values of l and α are allowed within $1-\sigma$. Thus, certain parameter space of the hairy Kerr scenario are less preferred compared to the Kerr scenario for Sgr A* within the domain of this model.

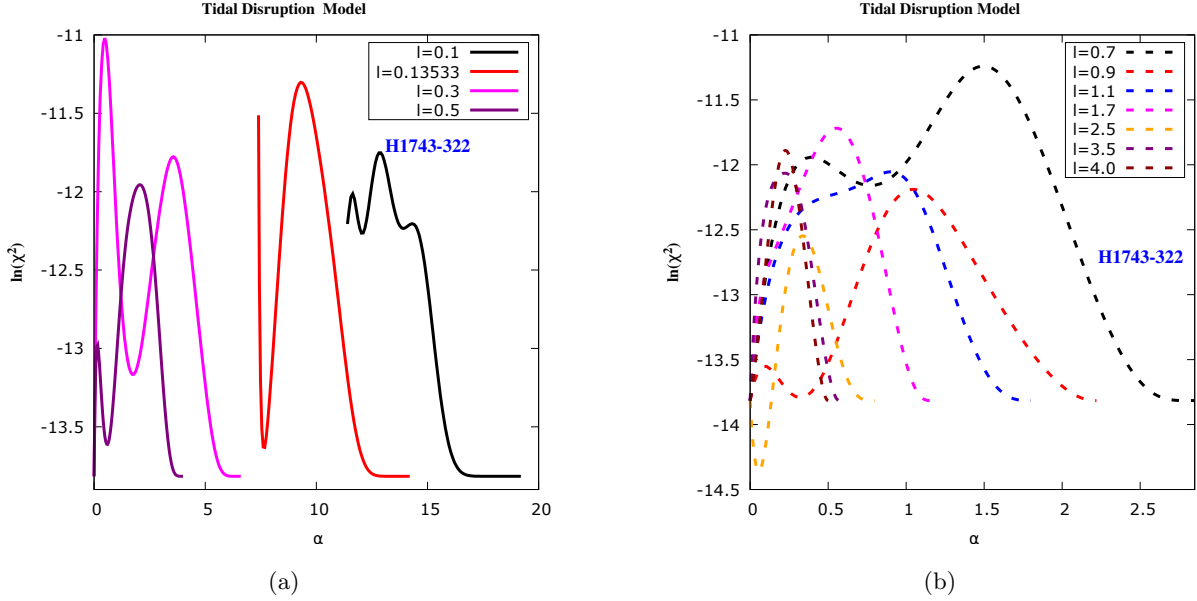


Figure 21: The above figure shows the variation of $\ln\chi^2$ with α for different choices of l when the TDM model is used to explain the HFQPOs of H 1743+322

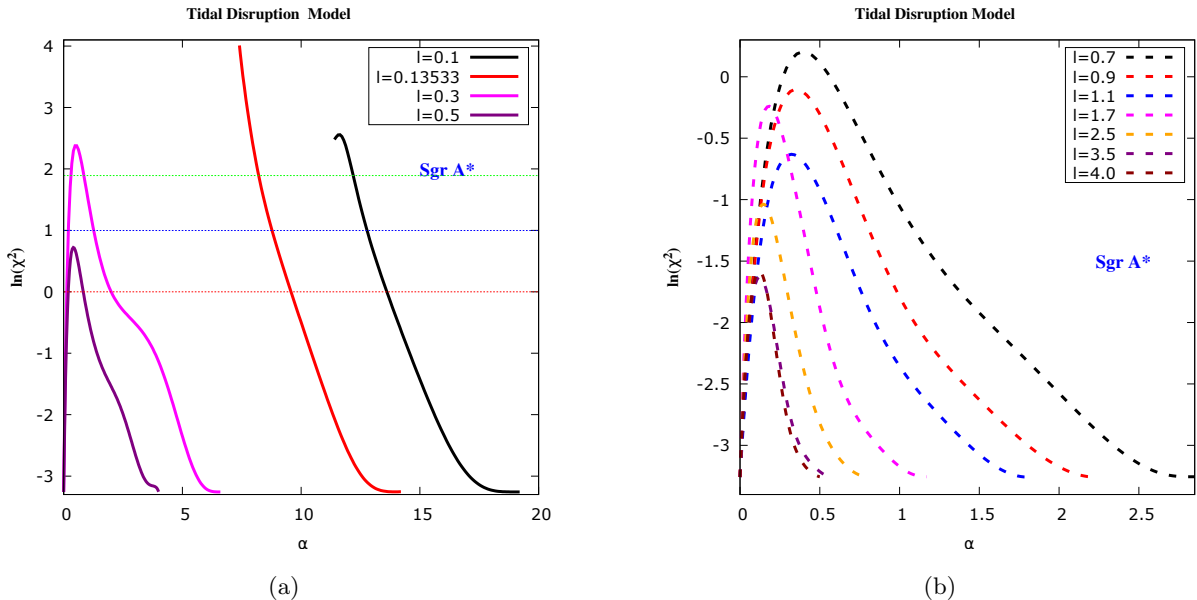


Figure 22: The above figure shows the variation of $\ln\chi^2$ with α for different choices of l when the RPM model is used to explain the HFQPO data of Sgr A*. The red, blue and green dotted lines are associated with the $1-\sigma$, $2-\sigma$ and $3-\sigma$ confidence intervals, which correspond to $\chi^2_{min} + 1$, $\chi^2_{min} + 2.71$ and $\chi^2_{min} + 6.63$ respectively.

3. XTE J1859+226

When the TDM is applied to fit the HFQPO data of XTE J1859+226, we observe from Fig. 23a that for $l = 0.1$ and $l = e^{-2}$ (i.e., $l \leq e^{-2}$), the corresponding χ^2 values rise sharply near α_{crit} . Consequently, for $l \sim 0.1$, the range $\alpha_{crit} \lesssim \alpha \lesssim 14$ is excluded at the $1-\sigma$ level, while $\alpha_{crit} \lesssim \alpha \lesssim 12$ is excluded at the $3-\sigma$ level. Likewise, for $l \sim e^{-2}$, the interval $\alpha_{crit} \lesssim \alpha \lesssim 10$ is ruled out at $1-\sigma$, and $\alpha_{crit} \lesssim \alpha \lesssim 8$ at $3-\sigma$. For intermediate values of l ($0.3 \lesssim l \lesssim 0.7$), the Kerr limit is favored, and the corresponding intermediate values of α are disfavored (see Fig. 23a). For larger values of l (Fig. 23b), although the χ^2 tends to peak at intermediate α for a fixed l , the peak values are not sufficiently large to exclude any portion of the l, α parameter space at

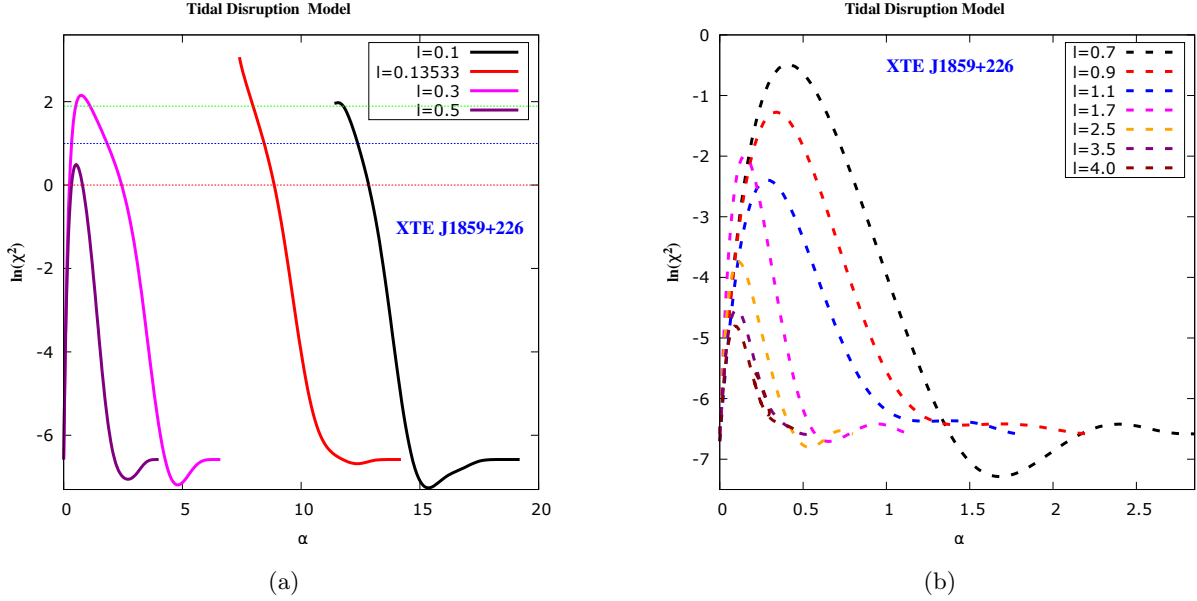


Figure 23: The above figure shows the variation of $\ln\chi^2$ with α for different choices of l when the RPM model is used to explain the HFQPO data of XTE J1859+226. The red, blue and green dotted lines are associated with the $1-\sigma$, $2-\sigma$ and $3-\sigma$ confidence intervals, which correspond to $\chi^2_{min} + 1$, $\chi^2_{min} + 2.71$ and $\chi^2_{min} + 6.63$ respectively.

the $1-\sigma$ level. Overall, within the framework of this model, parts of the hairy Kerr parameter space are less preferred than the Kerr solution for XTE J1859+226.

4.3 Model Comparison

In order to understand the relative importance of RPM or TDM in explaining the observed HFQPO frequencies of the six BH sources, we use the Akaike Information Criteria (AIC) [90] defined as:

$$AIC = -2 \ln \mathcal{L}_{max} + 2p, \quad (4.7)$$

where, \mathcal{L}_{max} represents the maximum likelihood and p the number of parameters in the model. The optimal model is the one that yields the lowest AIC value. In general, models with too few parameters fit the data poorly and therefore have lower log-likelihoods, whereas models with too many parameters are penalized by the second term in the AIC expression. Note that $-2 \ln \mathcal{L}_{max}$ corresponds to χ^2_{min} and therefore based on our previous analysis we can compare between RPM and TDM for each of the six BH sources. For both models, the number of parameters is $p = 5$, corresponding to l , α , a , M , and r_{cm} . Since both models have the same number of parameters AIC is purely determined by χ^2_{min} .

The AIC of a single model is not meaningful on its own; what matters is the comparison of AIC values across different models. Consequently, the model with the smallest AIC denoted as AIC_{min} is regarded as the best choice while the degree of evidential support for each model, relative to the others, can be determined with $\Delta_i = AIC_i - AIC_{min}$, where AIC_i represents the AIC of the i^{th} model. The model selection criteria corresponds to [91]:

1. $0 < \Delta_i \leq 2$: The i^{th} model and the most optimal model receives the same level of support.
2. $4 < \Delta_i \leq 10$: The i^{th} model has significantly less support compared to the optimal model.
3. $\Delta_i > 10$: Model i is essentially unsupported by the observational data.

From previous discussion we note that for GRO J1655-40, the magnitude of $\chi^2_{min} \sim 0$ for both the RPM and the TDM model. For GRO J1655-40, this becomes more explicit from the MCMC corner plot. Thus, $AIC_{TDM} = AIC_{RPM} \sim 5$ and both models are equally preferred by the source GRO J1655-40. However, the RPM model strongly favors the hairy Kerr scenario with $l \sim 0.1$, $\alpha \sim 12$ and rules out the Kerr model outside $3-\sigma$. Further, the spin of GRO J1655-40 predicted from the RPM assuming the Kerr scenario is $a_{min} \sim 0.3$

while for $l \sim 0.1, \alpha \sim 12, a_{min} \sim 0.28$ (see Sec. 4). This is not consistent with the spin of this source determined previously by other independent methods, e.g. the Continuum-Fitting method predicts $a \sim 0.65 - 0.75$ [92] while the Fe-line method predicts $a \sim 0.94 - 0.98$ [93]. Note that, the previous estimates of spin were made assuming the Kerr scenario and they are also not in mutual agreement. Assuming the Kerr scenario and TDM for its HFQPOs, the spin of GRO J1655-40 turns out to be $a_{min} \sim 0.1$. This spin also does not agree with at least one of the previous estimates. For TDM, the Kerr and the hairy Kerr scenario are equally favored. Thus, the spin of GRO J1655-40 predicted by the RPM and the TDM are not consistent with earlier estimates. Therefore, one needs to analyze other available HFQPO models to check the mutual consistency. Further, one may also consider revisiting the spin estimates of GRO J1655-40 assuming a non-Kerr background which might yield consistent values of spin and the hair parameter(s) from different methods.

For the source XTE J1550-564, Fig. 12 and Fig. 19 indicate that for both the RPM and TDM $\chi^2_{min} \sim 0$ and hence $AIC \sim 5$. Thus, both models seem to be equally favored by the HFQPO data for this source. Assuming the Kerr background, the observationally favored spin of this source corresponds to $a \sim 0.4$ (based on RPM) and $a \sim 0.3$ (based on TDM). Independent approaches—namely the Continuum-Fitting method, the Fe-line analysis and the jet power—have earlier yielded spin estimates of $a \sim 0.34$ (with an error bar of $-0.11 < a < 0.71$), $a = 0.55^{+0.15}_{-0.22}$, and $0.3 \lesssim a \lesssim 0.6$ [94] respectively [95]. Thus, both the models predict spins which are more or less consistent with earlier estimates. Hence, based on AIC or comparison with previous spin estimates, both RPM and TDM seem to be equally favored for the source XTE J1550-564.

For the source GRS 1915+105, from Fig. 13 and Fig. 20 we note that $\chi^2_{min} \sim 0$ and hence $AIC \sim 5$ for both the RPM and the TDM, indicating that both models are equally favored. Also, the data cannot distinguish the Kerr and the hairy Kerr scenario. Considering the Kerr background, the spin of GRS 1915+105 reported previously using different independent methods exhibit substantial variation. For example, the Fe-line analysis indicates a range of $a \sim 0.6 - 0.98$ [96], while the Continuum-Fitting method yields both intermediate values near $a \sim 0.7$ [97] and maximal spin at $a \sim 0.98$ [98]. More recent studies, which incorporate updated measurements of the mass and inclination of GRS 1915+105, place the spin in the interval $a \sim 0.4 - 0.98$ [99]. Spin values inferred from jet-power observations further suggest a range of $a \sim 0.6 - 0.9$ [94]. For $\alpha \sim 0$ in the hairy Kerr model, both RPM and TDM predict $a \lesssim 0.1$, which is not in agreement with any of the previous estimates based on independent methods. This may require revisiting the previous spin estimates of GRS 1915+105 by the Continuum-Fitting or the Fe-line method assuming a non-Kerr background. Further, one needs to compare the HFQPO data of GRS 1915+105 with other available HFQPO models, to arrive at the optimal model and also the spin estimates. We leave this for a future work which will be reported soon.

A similar conclusion also holds for the source H1743-322 when we compare Fig. 14 and Fig. 21, since $\chi^2_{min} \sim 0$ and χ^2 is insensitive to the variation in l, α such that the data fails to differentiate between the Kerr and the hairy Kerr scenario. For this source, assuming the Kerr geometry, RPM predicts $a_{min} \sim 0.5$ while TDM predicts $a_{min} \sim -0.1$. Using the Continuum-Fitting method, the spin of this source has been inferred to be $a = 0.2 \pm 0.3$ at the 68% confidence level, with a corresponding upper bound of $a < 0.92$ at 99.7% confidence [100]. An independent estimate derived from the observed jet power constrains the spin to lie in the range $0.25 \lesssim a \lesssim 0.5$ [94], in reasonable agreement with the Continuum-Fitting measurements reported in [100]. Since the spin predicted by RPM is in better agreement with [100], RPM seems to provide a better explanation of the HFQPO data of H1743-322, although the spin predicted by TDM is also within the error-bars.

Although the χ^2 exhibits substantial enhancement for smaller l and intermediate α , $\chi^2_{min} \sim 0$ for the source Sgr A* assuming both RPM and TDM (Fig. 15 and Fig. 22). Thus both models predict $AIC \sim 5$ and hence are equally favored. Earlier determinations of the spin of this source display considerable disparity, with some analyses supporting a nearly vanishing spin $a \lesssim 0.1$ [101], others indicating an intermediate value ($a \sim 0.5, a \sim 0.52, a \sim 0.22$) [102–104], and still others favoring a high to near-extremal spin ($a = 0.9 \pm 0.06, a \sim 0.92$) [105, 106]. These spins were determined assuming Sgr A* to be a Kerr BH. Here we assumed Sgr A* to be a hairy Kerr BH and based on RPM and TDM, the most favorable spins (assuming $\alpha \sim 0$) are $a_{min} \sim 0.92$ and $a_{min} \sim 0.8$, respectively, roughly in agreement with [105, 107]. Thus, the present data cannot differentiate between RPM and TDM, but the huge disparity in the earlier spin estimates possibly requires revisiting the spin estimates of this source by earlier independent methods assuming a non-Kerr geometry, e.g. the hairy Kerr scenario considered here.

Finally, when we compare Fig. 16 and Fig. 23 for XTE J1859+226, we note that $\chi^2_{min} \sim 0$ for both the RPM and the TDM, but for RPM χ^2 varies very sharply near the minima. This becomes more explicit from

the MCMC analysis, which yields $\chi^2_{min} \sim 0$ for this source assuming RPM (see Sec. 4.1.1). Thus, assuming the RPM this source strongly favors the hairy Kerr scenario with $l \sim 0.1$ and $\alpha \sim 12$ and rules out the Kerr scenario outside 3σ . But since $\chi^2_{min} \sim 0$ for both the RPM and the TDM, both models are equally favored, based on *AIC*. The spin of this object has been estimated using the relativistic precession model (RPM), yielding a low value of $a = 0.149 \pm 0.005$ [108]. This estimate is based on QPO data similar to the present analysis, and is consistent with the spin obtained in our RPM-based study. In contrast, spin measurements derived from other independent methods suggest a near-maximal value ($a = 0.987 \pm 0.003$) [109]. The spin of XTE J1859+226 predicted by the TDM in the present analysis assuming the Kerr geometry corresponds to $a_{min} \sim 0.9$ in better agreement with [109]. Thus, TDM seems to be a more plausible model when compared with RPM, to explain the HFQPO of XTE J1859+226. But, one needs to test the validity of the other HFQPO models for this source, which we leave for a future work.

5 Conclusion

In this work, we investigate the role of the hairy Kerr scenario in explaining the observed high frequency quasi-periodic oscillations (HFQPOs) in BH sources. Hairy black holes have garnered considerable interest, as they naturally arise in modified gravity theories, effective field frameworks, or within Einstein gravity coupled to additional self-interacting fields. Such BH solutions have been obtained by the method of extended gravitational decoupling [31] and are described by the deviation parameters α and l . The Kerr scenario is recovered either when $\alpha \rightarrow 0$ or when $l\alpha \rightarrow 2$. The rotating hairy black hole solution considered here satisfies the Einstein field equations with a conserved energy-momentum tensor that obeys the strong energy conditions (SECs). We investigate the horizon structure of the hairy Kerr BHs and report that the (α, l) parameter space can be classified into 3 domains: (a) $l \geq e^{-2}$, (b) $l = e^{-2}$ and (c) $l \leq e^{-2}$, manifesting certain interesting and unusual features, compared to the standard Kerr scenario. For certain choices of α and l there can be more than two horizons, for a given l the SEC is satisfied only above a critical α , and for any l , α can go only as high as $\alpha_{max} = 2/l$ to ensure asymptotic flatness. As $\alpha \rightarrow \alpha_{max}$, the Kerr limit is recovered. When $l = e^{-2}$ and $\alpha \simeq \alpha_{crit}$, the non-rotating BH is also the extremal BH and the horizon radius corresponds to the inflection point of the function $\Delta(l, \alpha, a, r)$ appearing in the metric. For $l > e^{-2}$ and $\alpha_{crit} \leq \alpha \leq \alpha_{coin} = 1/l$ the SEC is satisfied only in the spin range $0 \leq |a| \leq a_{SEC} < a_{max}$, while when $\alpha_{coin} < \alpha \leq \alpha_{max}$ all allowed spins satisfy the SEC. Based on the above classification we systematically study the radial variation of the three fundamental frequencies associated with the hairy Kerr spacetime. We also explore the sensitivity of the fundamental frequencies on the the deviation parameters (α, l) and also the BH spin and compare them with the Kerr scenario. This is important as we aim to test the viability of this solution in explaining the observed HFQPOs in BH sources, where the model dependent HFQPO frequencies depend on the three fundamental frequencies. This gives us an opportunity to constrain the parameter space of the hairy Kerr BH based on the available HFQPO observations.

Several theoretical models are proposed in the literature to explain the observed HFQPOs. Here, we consider the viability of the kinematic models of HFQPOs, namely, the Relativistic Precession Model (RPM) and the Tidal Disruption Model (TDM). We compare the model dependent QPO frequencies with the observed QPO frequencies of six available BH sources. Using χ^2 analysis, the parameter space of l and α is constrained based on RPM and TDM for each of the six BH sources. We also compare the performance of both the aforesaid models in explaining the HFQPO data of the six BH sources based on the Akaike Information Criterion and comparison with previous independent spin estimates.

For the sources GRS 1915+105, XTE J1550-564, H1743-322, and Sgr A* both the RPM and the TDM are equally favored. Also, for GRS 1915+105 and H1743-322 the data cannot distinguish the Kerr and the hairy Kerr scenario. Moreover, for XTE J1550-564 and Sgr A*, both the models predict spins which are more or less in agreement with earlier estimates. For the source GRS 1915+105, the predicted spins from RPM or TDM is much lower than all of the earlier independent estimates while for H1743-322, RPM seems to fare slightly better than TDM based on consistency with previous spin estimates. However, one may note that the spin of the same source estimated using different independent methods often exhibit substantial discrepancies. This, when coupled with the fact that the data often fails to distinguish the Kerr and the hairy Kerr scenario might indicate revisiting the previous spin measurements of these sources by the Continuum-Fitting or the Fe-line method assuming a non-Kerr background.

For the sources GRO J1655-40 and XTE J1859+226, assuming the RPM, the hairy Kerr scenario is more

preferred compared to the Kerr scenario since χ^2 attains a very sharp minima near $l \sim 0.1, \alpha \sim 12$. But since $\chi^2_{min} \sim 0$ for RPM, based on *AIC*, both the RPM and the TDM are equally favored. Moreover, the spin of these sources predicted from the RPM assuming the Kerr scenario is also not in agreement with the previous independent spin estimates. Note however, that the previous independent spin measurements made assuming the Kerr geometry, are also not in mutual agreement. The spin of XTE J1859+226 predicted from the TDM exhibits a better agreement with earlier estimates compared to the spin of GRO J1655-40 predicted from the TDM. Thus, considering the previous spin estimates, the TDM appears to be a more plausible model than the RPM for explaining the HFQPOs of XTE J1859+226. However for GRO J1655-40, both models do not seem to be that much suitable. Therefore, we need to analyze and compare other available HFQPO models to understand which is the most suitable model for each of these sources. We leave this for a future work which will be reported soon. The present analysis is limited by poor statistics, as only a few black hole sources exhibit HFQPOs, and by the lack of precise data. These limitations are expected to improve significantly with the ESA X-ray mission LOFT, enabling much tighter constraints on black hole spin and additional hairs from QPO based observations.

Acknowledgments

Research of I.B. is funded by the Start-Up Research Grant from SERB, DST, Government of India (Reg. No. SRG/2021/000418). The work of S. M. is supported by the core research grant from the Science and Engineering Research Board, a statutory body under the Department of Science and Technology, Government of India, under Grant Agreement No. CRG/2023/007670.

References

- [1] B. P. Abbott et al. Observation of gravitational waves from a binary black hole merger. *Phys. Rev. Lett.*, 116:061102, Feb 2016.
- [2] B. P. Abbott, R. Abbott, and et al Abbott. Gwtc-1: A gravitational-wave transient catalog of compact binary mergers observed by ligo and virgo during the first and second observing runs. *Phys. Rev. X*, 9:031040, Sep 2019.
- [3] B. P. Abbott et al. GW170817: Observation of Gravitational Waves from a Binary Neutron Star Inspiral. *Phys. Rev. Lett.*, 119(16):161101, 2017.
- [4] et al Akiyama. First m87 event horizon telescope results. i. the shadow of the supermassive black hole. *The Astrophysical Journal Letters*, 875(1):L1, April 2019.
- [5] Kazunori Akiyama et al. First Sagittarius A* Event Horizon Telescope Results. I. The Shadow of the Supermassive Black Hole in the Center of the Milky Way. *Astrophys. J. Lett.*, 930(2):L12, 2022.
- [6] J.A. Wheeler R.Ruffini. Introducing to black hole. *Phys.Rev B*, 24, 1971.
- [7] Jacob D. Bekenstein. Nonexistence of baryon number for static black holes. *Phys. Rev. D*, 5:1239–1246, 1972.
- [8] J. D. Bekenstein. Novel “no-scalar-hair” theorem for black holes. *Phys. Rev. D*, 51(12):R6608, 1995.
- [9] D. Sudarsky. A Simple proof of a no hair theorem in Einstein Higgs theory,. *Class. Quant. Grav.*, 12:579–584, 1995.
- [10] Carlos A. R. Herdeiro and Eugen Radu. Asymptotically flat black holes with scalar hair: a review. *Int. J. Mod. Phys. D*, 24(09):1542014, 2015.
- [11] Thomas Hertog. Towards a Novel no-hair Theorem for Black Holes. *Phys. Rev. D*, 74:084008, 2006.
- [12] NM Bocharova, KA Bronnikov, and VN Melnikov. An exact solution of the system of einstein equations and mass-free scalar field. *Vestn. Mosk. Univ. Fiz. Astro*, 6:706, 1970.

- [13] J.D. Bekenstein. Exact solutions of Einstein conformal scalar equations. *Annals Phys.*, 82:535, 1974.
- [14] J.D. Bekenstein. Black Holes with Scalar Charge. *Annals Phys.*, 91:75, 1975.
- [15] K.A. Bronnikov and Yu.N. Kireev. Instability of Black Holes with Scalar Charge. *Phys. Lett. A*, 67:95, 1978.
- [16] Takashi Torii, Kengo Maeda, and Makoto Narita. Toward the no-scalar-hair conjecture in asymptotically de sitter spacetime. *Physical Review D*, 59(6):064027, 1999.
- [17] Konstantin G Zloshchastiev. Coexistence of black holes and a long-range scalar field in cosmology. *Physical review letters*, 94(12):121101, 2005.
- [18] Emanuele Berti, Vitor Cardoso, Leonardo Gualtieri, Michael Horbatsch, and Ulrich Sperhake. Numerical simulations of single and binary black holes in scalar-tensor theories: circumventing the no-hair theorem. *Physical Review D*, 87(12):124020, 2013.
- [19] David Garfinkle, Gary T Horowitz, and Andrew Strominger. Charged black holes in string theory. *Physical Review D*, 43(10):3140, 1991.
- [20] Othmar Brodbeck and Norbert Straumann. Instability proof for einstein-yang-mills solitons and black holes with arbitrary gauge groups. *Journal of Mathematical Physics*, 37(3):1414–1433, 1996.
- [21] MS Volkov, O Brodbeck, G Lavrelashvili, and N Straumann. The number of sphaleron instabilities of the bartnik-mckinnon solitons and non-abelian black holes. *Physics Letters B*, 349(4):438–442, 1995.
- [22] Piotr Bizon and Robert M Wald. The $n=1$ colored black hole is unstable. *Physics Letters B*, 267(2):173–174, 1991.
- [23] Piotr Bizon. Stability of einstein yang-mills black holes. *Physics Letters B*, 259(1-2):53–57, 1991.
- [24] Zhi-hong Zhou and Norbert Straumann. Nonlinear perturbations of einstein-yang-mills solitons and non-abelian black holes. *Nuclear Physics B*, 360(1):180–196, 1991.
- [25] Piotr Bizon. Colored black holes. *Physical review letters*, 64(24):2844, 1990.
- [26] Subhash Mahapatra, Supragyan Priyadarshinee, Gosala Narasimha Reddy, and Bhaskar Shukla. Exact topological charged hairy black holes in AdS Space in D -dimensions. *Phys. Rev. D*, 102(2):024042, 2020.
- [27] Supragyan Priyadarshinee, Subhash Mahapatra, and Indrani Banerjee. Analytic topological hairy dyonic black holes and thermodynamics. *Phys. Rev. D*, 104(8):084023, 2021.
- [28] Supragyan Priyadarshinee and Subhash Mahapatra. Analytic three-dimensional primary hair charged black holes and thermodynamics. *Phys. Rev. D*, 108(4):044017, 2023.
- [29] Jorge Ovalle. Decoupling gravitational sources in general relativity: from perfect to anisotropic fluids. *Phys. Rev. D*, 95(10):104019, 2017.
- [30] J. Ovalle. Decoupling gravitational sources in general relativity: The extended case. *Phys. Lett. B*, 788:213–218, 2019.
- [31] J. Ovalle, R. Casadio, E. Contreras, and A. Sotomayor. Hairy black holes by gravitational decoupling. *Phys. Dark Univ.*, 31:100744, 2021.
- [32] J. Ovalle, R. Casadio, R. da Rocha, A. Sotomayor, and Z. Stuchlik. Black holes by gravitational decoupling. *Eur. Phys. J. C*, 78(11):960, 2018.
- [33] J. Ovalle, R. Casadio, R. da Rocha, and A. Sotomayor. Anisotropic solutions by gravitational decoupling. *Eur. Phys. J. C*, 78(2):122, 2018.
- [34] V. A. Torres-Sánchez and Ernesto Contreras. Anisotropic neutron stars by gravitational decoupling. *Eur. Phys. J. C*, 79(10):829, 2019.

[35] Piyachat Panyasiripan, Narakorn Kaewkhao, Phongpichit Channuie, and Ali Övgün. Traversable wormholes in minimally geometrical deformed trace-free gravity using gravitational decoupling. *Nucl. Phys. B*, 1004:116563, 2024.

[36] Roberto Casadio, Jorge Ovalle, and Roldão da Rocha. The Minimal Geometric Deformation Approach Extended. *Class. Quant. Grav.*, 32(21):215020, 2015.

[37] Maxim Misyura, Angel Rincon, and Vitalii Vertogradov. Non-singular black hole by gravitational decoupling and some thermodynamic properties. *Phys. Dark Univ.*, 46:101717, 2024.

[38] Yaobin Hua, Zhenglong Ban, Tian-You Ren, Jia-Jun Yin, and Rong-Jia Yang. Regular hairy black holes through gravitational decoupling method. 10 2025.

[39] Subhash Mahapatra and Indrani Banerjee. Rotating hairy black holes and thermodynamics from gravitational decoupling. *Phys. Dark Univ.*, 39:101172, 2023.

[40] M. Sharif and Amal Majid. Extended gravitational decoupled solutions in self-interacting Brans–Dicke theory. *Phys. Dark Univ.*, 30:100610, 2020.

[41] J. Ovalle, R. Casadio, R. da Rocha, A. Sotomayor, and Z. Stuchlik. Black holes by gravitational decoupling. *The European Physical Journal C*, 78(11), November 2018.

[42] E. Contreras, J. Ovalle, and R. Casadio. Gravitational decoupling for axially symmetric systems and rotating black holes. *Physical Review D*, 103(4), February 2021.

[43] Shafqat Ul Islam and Sushant G. Ghosh. Strong field gravitational lensing by hairy kerr black holes. *Phys. Rev. D*, 103:124052, Jun 2021.

[44] Misba Afrin, Rahul Kumar, and Sushant G. Ghosh. Parameter estimation of hairy Kerr black holes from its shadow and constraints from M87*. *Mon. Not. Roy. Astron. Soc.*, 504:5927–5940, 2021.

[45] Vitalii Vertogradov and Dmitriy Kudryavcev. On the temperature of hairy black holes. 3 2023.

[46] Shafqat Ul Islam and Sushant G. Ghosh. Strong field gravitational lensing by hairy Kerr black holes. *Phys. Rev. D*, 103(12):124052, 2021.

[47] Zhen-Hao Yang, Liang-Bi Wu, Xiao-Mei Kuang, and Wei-Liang Qian. QNM families: classification and competition. 10 2025.

[48] Yuan Meng, Xiao-Mei Kuang, Xi-Jing Wang, Bin Wang, and Jian-Pin Wu. Images from disk and spherical accretions of hairy Schwarzschild black holes. *Phys. Rev. D*, 108(6):064013, 2023.

[49] Yuan Meng, Xi-Jing Wang, Yong-Zhuang Li, and Xiao-Mei Kuang. Effects of hair on the image of a rotating black hole illuminated by a thin accretion disk. *Eur. Phys. J. C*, 85(6):627, 2025.

[50] Riasat Ali, Xia Tiecheng, Muhammad Awais, and Rimsha Babar. Study of light deflection and shadow from a hairy black hole under the influence of the non-magnetic plasma. *Chin. J. Phys.*, 94:416–430, 2025.

[51] V. F. Guimarães, R. T. Cavalcanti, and R. da Rocha. Hair imprints of the gravitational decoupling and hairy black hole spectroscopy. *Class. Quant. Grav.*, 42(17):175011, 2025.

[52] Sunny Vagnozzi et al. Horizon-scale tests of gravity theories and fundamental physics from the Event Horizon Telescope image of Sagittarius A. *Class. Quant. Grav.*, 40(16):165007, 2023.

[53] Xi-Jing Wang, Yuan Meng, Xiao-Mei Kuang, and Kai Liao. Exploring black holes with multiple photon spheres by interferometric signatures. 8 2025.

[54] Vitalii Vertogradov and Ali Övgün. Analyzing the influence of geometrical deformation on photon sphere and shadow radius: A new analytical approach — Spherically symmetric spacetimes. *Phys. Dark Univ.*, 45:101541, 2024.

[55] Zhen Li and Faqiang Yuan. Energy extraction via Comisso-Asenjo mechanism from rotating hairy black hole. *Phys. Rev. D*, 108(2):024039, 2023.

[56] Zhen Li. Superradiance and quasinormal modes of the gravitational perturbation around rotating hairy black hole. *Phys. Lett. B*, 841:137902, 2023.

[57] Yaghoub Heydarzade, Maxim Misura, and Vitalii Vertogradov. Hairy Kiselev black hole solutions. *Phys. Rev. D*, 108(4):044073, 2023.

[58] Ahmad Al-Badawi, Sohan Kumar Jha, and Anisur Rahaman. The fermionic greybody factor and quasi-normal modes of hairy black holes, as well as Hawking radiation's power spectrum and sparsity. *Eur. Phys. J. C*, 84(2):145, 2024.

[59] G. Mustafa, Faisal Javed, S. K. Maurya, A. Ditta, Orhan Donmez, Tayyab Naseer, Abdelmalek Bouzenada, and Farruh Atamurotov. Magnetized particle motion and accretion process with shock cone morphology around a decoupled hairy black holes. 11 2025.

[60] M. van der Klis. Millisecond oscillations in x-ray binaries. *Ann. Rev. Astron. Astrophys.*, 38:717–760, 2000.

[61] Andrea Maselli, Leonardo Gualtieri, Paolo Pani, Luigi Stella, and Valeria Ferrari. Testing Gravity with Quasi Periodic Oscillations from accreting Black Holes: the Case of the Einstein-Dilaton-Gauss-Bonnet Theory. *Astrophys. J.*, 801(2):115, 2015.

[62] T. M. Tauris and E. P. J. van den Heuvel. Formation and evolution of compact stellar X-ray sources. In Walter H. G. Lewin and Michiel van der Klis, editors, *Compact stellar X-ray sources*, volume 39, pages 623–665. 2006.

[63] Gabriel Torok. A Possible 3:2 orbital epicyclic resonance in QPOs frequencies of Sgr A*. *Astron. Astrophys.*, 440:1, 2005.

[64] Marek A. Abramowicz and P. Chris Fragile. Foundations of Black Hole Accretion Disk Theory. *Living Rev. Rel.*, 16:1, 2013.

[65] B. Aschenbach. Measuring mass and angular momentum of black holes with high-frequency quasiperiodic oscillations. *Astron. Astrophys.*, 425:1075–1082, 2004.

[66] Gabriel Torok, Andrea Kotrlova, Eva Sramkova, and Zdenek Stuchlik. Confronting the models of 3:2 quasiperiodic oscillations with the rapid spin of the microquasar GRS 1915+105. *Astron. Astrophys.*, 531:A59, 2011.

[67] V. F. Shvartsman. Halos around “Black Holes”. *sovast*, 15:377, December 1971.

[68] R. A. Syunyaev. Variability of X Rays from Black Holes with Accretion Disks. *sovast*, 16:941, June 1973.

[69] Luigi Stella and Mario Vietri. khz quasiperiodic oscillations in low-mass x-ray binaries as probes of general relativity in the strong-field regime. *Phys. Rev. Lett.*, 82:17–20, Jan 1999.

[70] Walter H. G. Lewin and Michiel van der Klis. *Compact Stellar X-ray Sources*, volume 39. 2006.

[71] Alireza Allahyari and Lijing Shao. Testing no-hair theorem by quasi-periodic oscillations: the quadrupole of GRO J1655–40. *JCAP*, 10:003, 2021.

[72] Xin Jiang, Peng Wang, Haitang Yang, and Houwen Wu. Testing Kerr black hole mimickers with quasi-periodic oscillations from GRO J1655-40. *Eur. Phys. J. C*, 81(11):1043, 2021. [Erratum: Eur.Phys.J.C 82, 5 (2022)].

[73] Anirban Dasgupta and Indrani Banerjee. Constraining the rotating Simpson-Visser spacetime from the observed quasiperiodic oscillations in black holes. *Phys. Rev. D*, 112(12):124018, 2025.

[74] Anirban Dasgupta, Nishant Tiwari, and Indrani Banerjee. Signatures of Einstein-Maxwell dilaton-axion gravity from the observed quasi-periodic oscillations in black holes. *JCAP*, 10:054, 2025.

[75] Indrani Banerjee. Deciphering signatures of Bardeen black holes from the observed quasi-periodic oscillations. *JCAP*, 05(05):020, 2022.

[76] Cheng Liu, Hoongwah Siew, Tao Zhu, Qiang Wu, Yuanyuan Zhao, and Haiguang Xu. Constraints on Hairy Kerr black hole with quasi-periodic oscillations. 11 2023.

[77] Martin E Beer and Philipp Podsiadlowski. The quiescent light curve and the evolutionary state of gro j1655–40. *Monthly Notices of the Royal Astronomical Society*, 331(2):351–360, 2002.

[78] SE Motta, TM Belloni, L Stella, T Muñoz-Darias, and R Fender. Precise mass and spin measurements for a stellar-mass black hole through x-ray timing: the case of gro j1655- 40. *Monthly Notices of the Royal Astronomical Society*, 437(3):2554–2565, 2014.

[79] Jerome A. Orosz, James F. Steiner, Jeffrey E. McClintock, Manuel A. P. Torres, Ronald A. Remillard, Charles D. Bailyn, and Jon M. Miller. An Improved Dynamical Model for the Microquasar XTE J1550-564. *Astrophys. J.*, 730:75, 2011.

[80] M. J. Reid, J. E. McClintock, J. F. Steiner, D. Steeghs, R. A. Remillard, V. Dhawan, and R. Narayan. A Parallax Distance to the Microquasar GRS 1915+105 and a Revised Estimate of its Black Hole Mass. *Astrophys. J.*, 796:2, 2014.

[81] Guancheng Pei, Sourabh Nampalliwar, Cosimo Bambi, and Matthew J. Middleton. Blandford-Znajek mechanism in black holes in alternative theories of gravity. *Eur. Phys. J. C*, 76(10):534, 2016.

[82] Ayan Bhattacharjee, Indrani Banerjee, Anuvab Banerjee, Dipak Debnath, and Sandip K. Chakrabarti. The 2004 Outburst of BHC H1743-322: Analysis of spectral and timing properties using the TCAF Solution. *Mon. Not. Roy. Astron. Soc.*, 466:1372–1381, 2017.

[83] J. Petri. A new model for QPOs in accreting black holes: application to the microquasar GRS 1915+105. *Astrophys. Space Sci.*, 318:181–186, 2008.

[84] A. M. Ghez et al. Measuring Distance and Properties of the Milky Way’s Central Supermassive Black Hole with Stellar Orbits. *Astrophys. J.*, 689:1044–1062, 2008.

[85] S. Gillessen, F. Eisenhauer, S. Trippe, T. Alexander, R. Genzel, F. Martins, and T. Ott. Monitoring stellar orbits around the Massive Black Hole in the Galactic Center. *Astrophys. J.*, 692:1075–1109, 2009.

[86] Zdeněk Stuchlík and Andrea Kotrlová. Orbital resonances in discs around braneworld Kerr black holes. *Gen. Rel. Grav.*, 41:1305–1343, 2009.

[87] SE Motta, T Belloni, L Stella, Georgios Pappas, J Casares, AT Muñoz-Darias, MAP Torres, and IV Yanes-Rizo. Black hole mass and spin measurements through the relativistic precession model: Xte j1859+ 226. *Monthly Notices of the Royal Astronomical Society*, 517(1):1469–1475, 2022.

[88] Yoram Avni. Energy spectra of x-ray clusters of galaxies. *Astrophysical Journal, vol. 210, Dec. 15, 1976, pt. 1, p. 642-646. Research supported by the Israel Academy of Sciences and Humanities and Science Research Council*, 210:642–646, 1976.

[89] Licia Verde. Statistical methods in cosmology. *Lect. Notes Phys.*, 800:147–177, 2010.

[90] H. Akaike. A new look at the statistical model identification. *IEEE Transactions on Automatic Control*, 19(6):716–723, 1974.

[91] Shining Yang, Jianbo Lu, Xinpeng Yu, and Jingyang Xu. Study on high-frequency quasi-periodic oscillations in rotating black bounce spacetime. *Class. Quant. Grav.*, 42(4):045006, 2025.

[92] Rebecca Shafee, Jeffrey E McClintock, Ramesh Narayan, Shane W Davis, Li-Xin Li, and Ronald A Remillard. Estimating the spin of stellar-mass black holes by spectral fitting of the x-ray continuum. *The Astrophysical Journal*, 636(2):L113, 2005.

[93] J. M. Miller, C. S. Reynolds, A. C. Fabian, G. Miniutti, and L. C. Gallo. Stellar-mass Black Hole Spin Constraints from Disk Reflection and Continuum Modeling. *Astrophys. J.*, 697:900–912, 2009.

[94] Indrani Banerjee, Bhaswati Mandal, and Soumitra SenGupta. Signatures of Einstein-Maxwell dilaton-axion gravity from the observed jet power and the radiative efficiency. *Phys. Rev. D*, 103(4):044046, 2021.

[95] James F Steiner, Rubens C Reis, Jeffrey E McClintock, Ramesh Narayan, Ronald A Remillard, Jerome A Orosz, Lijun Gou, Andrew C Fabian, and Manuel AP Torres. The spin of the black hole microquasar xte j1550- 564 via the continuum-fitting and fe-line methods. *Monthly Notices of the Royal Astronomical Society*, 416(2):941–958, 2011.

[96] J. L. Blum, J. M. Miller, A. C. Fabian, M. C. Miller, J. Homan, M. van der Klis, E. M. Cackett, and R. C. Reis. Measuring the Spin of GRS 1915+105 with Relativistic Disk Reflection. *Astrophys. J.*, 706:60–66, 2009.

[97] Matthew Middleton, Chris Done, Marek Gierliński, and Shane W. Davis. Black hole spin in GRS 1915+105. *mnras*, 373(3):1004–1012, December 2006.

[98] Jeffrey E. McClintock, Rebecca Shafee, Ramesh Narayan, Ronald A. Remillard, Shane W. Davis, and Li-Xin Li. The Spin of the Near-Extreme Kerr Black Hole GRS 1915+105. *Astrophys. J.*, 652:518–539, 2006.

[99] Brianna S. Mills, Shane W. Davis, and Matthew J. Middleton. The Black Hole Spin in GRS 1915+105, Revisited. *Astrophys. J.*, 914(1):6, 2021.

[100] James F. Steiner, Jeffrey E. McClintock, and Mark J. Reid. The Distance, Inclination, and Spin of the Black Hole Microquasar H1743-322. *Astrophys. J. Lett.*, 745:L7, 2012.

[101] Giacomo Fragione and Abraham Loeb. An upper limit on the spin of SgrA* based on stellar orbits in its vicinity. *Astrophys. J. Lett.*, 901(2):L32, 2020.

[102] R. Genzel, R. Schodel, Thomas Ott, A. Eckart, T. Alexander, F. Lacombe, D. Rouan, and B. Aschenbach. Near-infrared flares from accreting gas around the supermassive black hole at the galactic centre. *Nature*, 425:934–937, 2003.

[103] Roman V. Shcherbakov, Robert F. Penna, and Jonathan C. McKinney. Sagittarius A* Accretion Flow and Black Hole Parameters from General Relativistic Dynamical and Polarized Radiative Modeling. *Astrophys. J.*, 755:133, 2012.

[104] Guillaume Belanger, Regis Terrier, Okkie C. De Jager, Andrea Goldwurm, and Fulvio Melia. Periodic Modulations in an X-ray Flare from Sagittarius A*. *J. Phys. Conf. Ser.*, 54:420–426, 2006.

[105] Ruth A. Daly, Megan Donahue, Christopher P. O’Dea, Biny Sebastian, Daryl Haggard, and Anan Lu. New black hole spin values for Sagittarius A* obtained with the outflow method. *Mon. Not. Roy. Astron. Soc.*, 527(1):428–436, 2023.

[106] Monika Moscibrodzka, Charles F. Gammie, Joshua C. Dolence, Hotaka Shiokawa, and Po Kin Leung. Radiative Models of Sgr A* from GRMHD Simulations. *Astrophys. J.*, 706:497–507, 2009.

[107] Leonhard Meyer, A. Eckart, R. Schoedel, W. J. Duschl, K. Muzic, M. Dovciak, and V. Karas. Near-infrared polarimetry setting constraints on the orbiting spot model for Sgr A* flares. *Astron. Astrophys.*, 460:15, 2006.

[108] S. E. Motta, T. Belloni, L. Stella, G. Pappas, J. A. Casares, A. T. Muñoz-Darias, M. A. P. Torres, and I. V. Yanes-Rizo. Black hole mass and spin measurements through the relativistic precession model: XTE J1859+226. *Mon. Not. Roy. Astron. Soc.*, 517(1):1469–1475, 2022.

[109] Gitika Mall, Honghui Liu, Cosimo Bambi, James F. Steiner, and Javier A. Garcia. Measuring Black Hole Spins through X-ray Reflection Spectroscopy and the Relativistic Precession Model: the case of XTE J1859+226. *Mon. Not. Roy. Astron. Soc.*, 527:12053–12064, 2024.